



WPI

Thermal and Electrical Transport Measurements in Wrought and Cast Aluminum Alloys

A Major Qualifying Project
Submitted to the Faculty
Of the
WORCESTER POLYTECHNIC INSTITUTE
In Partial Fulfillment of the Requirements for the
Degree of Bachelor of Science

By

Lydia D. George

Charles B. Plummer

Daniela Ruiz

Xiaoyu Wang

April 30, 2015

Advisors

Professor Germano S. Iannacchione

Professor Diana A. Lados

Abstract

Transport properties are essential considerations in the selection of a material for critical transportation and energy applications. In this project, relationships between materials' microstructure and micro-hardness and their thermal and electrical conductivities have been developed. Three aluminum alloys (wrought 6061 and cast 319 and A356) with various secondary dendrite arm spacing (SDAS = 60 μm and 100 μm), eutectic Si morphology (unmodified and Sr-modified), and aging conditions (natural aging and various artificial aging times) have been selected for the studies. Thermal conductivity was investigated using a custom-built apparatus applying a DC method, while the electrical resistivity used a four-wire Digital Multimeter (DMM) method. All alloys' microstructures were observed and quantified using an optical microscope with image analysis, and the α -Al matrix resistance was evaluated using Vickers micro-hardness tests. Conductivity results were uniquely correlated to the materials' characteristic microstructures and aging conditions, and the observed behavior/trends will be presented and discussed.

Table of Contents

Abstract.....	2
List of Figures.....	5
Chapter 1: Introduction, Background and Literature Review.....	8
1.1 Objectives	8
1.2 Principles of Transport Phenomena	9
1.3 Literature Review.....	12
Chapter 2: Methodology	15
2.1 Materials and Processing	15
2.2 Heat Treatment and Precipitation Strengthening.....	23
2.2 Literature Review Relevant to the Relationships between Transport Properties and Materials Microstructures	26
2.4 Apparatus: Design and Fabrication.....	36
2.5 Test Specimen Geometry	38
Chapter 3: Measuring Methods.....	41
3.1 Transport Equations.....	41
3.1.1 Thermal Conductivity Equations	41
3.1.2 Electrical Conductivity Equations.....	44
3.2 Thermal Conductivity Measurements.....	46
3.2.1 Original Testing Procedure	46
3.2.2 Modified Testing Procedure.....	46

3.3 Electrical Conductivity Measurements	48
3.4 Data Collection and Analysis.....	48
Chapter 4: Results and Discussion.....	49
4.1 Effects of Aging Time on Thermal and Electrical Conductivities.....	49
4.2 Effects of SDAS on Thermal Conductivity	50
4.3 Effects of Eutectic Si Modification on Thermal Conductivity	51
4.4 Correlation between Thermal Conductivity and Microhardness	52
4.5 Eutectic Particle Size and Shape Factor Relationships to Thermal Conductivity.....	53
Chapter 5: Conclusions, Recommendations and Future Work	56
5.1 Conclusions.....	56
5.2 Recommendations and Future Work.....	56
References.....	58

List of Figures

Figure 1. Thermal conductivity plotted against the electrical conductivity (Smith, 1935).....	10
Figure 2. Comparative cut bar set-up method (Principal Methods of Thermal Conductivity Measurement, 2014).....	12
Figure 3. Searle's bar method apparatus for measuring thermal conductivity.	13
Figure 4. Al-Si phase diagram for 6061, 319, and A356.	17
Figure 5. Optical micrograph showing grain boundaries of rolled 6061.	18
Figure 6. An image of dendrites (Introduction to Metallography, 2014).....	18
Figure 7. Theoretical dendrite growth pattern (Malekan & Shabestari, 2009).	19
Figure 8. Diagram showing the length that describe the morphology of primary dendrites (a) the relationship between the primary dendrite size and the average length of the silicon phase (b), and the relationship between spacing and diameter of silicon (c) (Shabani, Mazahery, Bahmani, Davami, & Varahram, 2010).	20
Figure 9. Solidification rate vs. secondary dendrite arm spacing (Vazquez-Lopez, 1999).	21
Figure 10. Microstructures of studied 6061, 319, and A356 alloys.....	22
Figure 11. Top row: shape factor; bottom row: particle diameter (for 319 and A356 alloys).	23
Figure 12. Heat treatment procedures for 6061, 319, and A356.....	24
Figure 14. Strength and precipitate growth of aluminum 6061 with regards to aging time.	25
Figure 15. Secondary dendrite arm spacing vs. thermal conductivity in A319 aluminum (Vazquez-Lopez, 1999).	26
Figure 16. Dendrite perimeter vs. thermal conductivity in A319 aluminum (Vazquez-Lopez, 1999).	27
Figure 17. The effect of cooling rate on electrical resistivity (Grandfield & Eskin, 2013).	27
Figure 18. Thermal conductivity of Al 6061 and SiC _p /6061 Al composite measured as a function	28
Figure 19. Electrical conductivity and hardness values of artificially and naturally-aged samples in (a) T6 and (b) T5 conditions (Cerri, E., et al., 2000).	30

Figure 20: Variation in impact strength with section size (Akhil, K., et al., 2014).	31
Figure 21. Variation in hardness with section size (Akhil, K., et al., 2014).	32
Figure 22. Variation of (a) electrical conductivity and (b) thermal conductivity with temperature for pure aluminum, 319, and A356 (Bakhtiyarov, S. I., et al., 2001).	33
Figure 23: Electrical conductivity at T4 condition of unmodified and modified A356 coupons upon solution treatment at 540°C (Hernandez, Paz J., 2003).	34
Figure 24. Schematic of apparatus.	37
Figure 25. Apparatus used for thermal conductivity measurements.	38
Figure 26. Dimensions of the three pure aluminum test samples.	39
Figure 27. Plot of an Al 319 sample, showing the change in temperature with elapsing time before testing (while waiting for steady-state).....	47
Figure 28. Four wire electrical measurement setup.	48
Figure 29. Relationship between thermal conductivity and aging in all alloys.	49
Figure 30. Relationship between electrical conductivity and aging time in 6061.	50
Figure 31. Relationship between thermal conductivity and SDAS in A356.....	51
Figure 32. Relationship between thermal conductivity and Sr modification in A319.	51
Figure 33. Relationship between thermal conductivity and Sr modification in A356.	52
Figure 34. Relationship between thermal conductivity and microhardness in 6061.....	52
Figure 35. Shape of indentation side view and top view in a typical Vickers microhardness test (Callister, 2000).	53
Figure 36. Relationship between thermal conductivity and eutectic Si particle size for 319 and A356 cast alloys.	54
Figure 37. Relationship between thermal conductivity and eutectic Si shape factor for 319 and A356 cast alloys.	55

List of Tables

Table 1. Chemical compositions of aluminum 6061, 319, and A356.....	16
Table 2. Important properties of aluminum alloys.....	17
Table 3. Table of solution heat treatment and artificial aging	24
Table 4. Density and electrical conductivity with regards to Sr content (Manzano-Ramirez 1993)	35
Table 5: Density and electrical conductivity of unmodified Al-Si melts (Manzano-Ramirez 1993)	36
Table 6. Sample characteristics.....	40
Table 7. Summary equations for thermal conductivity calculations.....	44
Table 8. Summary equations for electrical conductivity calculations	45
Table 9. Particle size and shape factor of 319 and A356 alloys	54

Chapter 1: Introduction, Background and Literature Review

Currently, during the material selection process, every material is characterized with an intrinsic thermal and electrical conductivity. However it has been experimentally shown that these transport characteristics are not only dependent on the composition of the material but also the microstructure. These differences are most apparent in the various processing methods used for metal alloys.

Thus, a need exists within the field of material science to gain a deeper understanding of this transport phenomena. Should a better model be developed, there are a large number of industrial implications, including engine design, electronic equipment design, and the creation of insulation materials, which pose to make significant advances. For example, engine efficiency is partially based off of the removal of heat. Thus by better understanding heat transport, better materials or material structures may be selected. Similarly, the cooling of electronics equipment and the conductance of electrical in circuitry is vital to the design of electronics. By improving material selection, small electronics may be built with faster speeds. Finally, a third type of industry that would benefit from this would be those which rely on insulation, whether it be fire protection, electronics, or laboratories. By designing more resistive materials, better insulation, with potentially thinner materials may be created. On the other hand, engine efficiency is currently limited by the ability of the engine materials to dissipate heat, and material thermal management is a critical consideration for design. Developing knowledge necessary to optimize the material/process for thermal applications in transportation is thus very important.

1.1 Objectives

The goal of this study is to make correlations between the thermal and electrical conductivities of 6061, A356, and 319 alloys and their microstructure and mechanical properties. To make these correlations, a number of objectives were made to accomplish the aim of the study. These objectives were to select and study aluminum alloys typically used in engine and structural applications, develop and validate an experimental methodology to evaluate materials' thermal and electrical conductivities, correlate microstructural characteristics to these properties in order to develop a fundamental material science understanding, and optimize processing and post-processing conditions for thermal transport applications. Ultimately, these objectives will aid in developing knowledge that is necessary to optimize the material and material processing for thermal applications in transportation.

1.2 Principles of Transport Phenomena

Electrical conductivity measures the ability of a material to conduct an electric current. In resistors and conductors, if there is an electric field, an electric current will flow through the material. The electrical resistivity is the ratio of the electric field to the density of the current and is represented by

$$\sigma = \frac{1}{\rho} = \frac{J}{E}, \quad (1)$$

where ρ is the resistivity of the conductor material, E is the magnitude of the electric field and J is the magnitude of the current density.

Conductivity results differently between materials, such as metals and insulators. A metal contains a lattice of atoms with an outer shell of electrons that travel through the lattice. The electrons allow the metal to conduct electric current. Conductors with a large cross-sectional area contain more electrons to carry the current. In semiconductors and insulators, donor atoms, which alter the electrical properties of a material, donate electrons to the conduction band or accept holes in the valence band, resulting in the change of the carrier concentration. This event causes the resistance to decrease (Nave, Resistance and Resistivity, 1998).

Thermal conductivity measures the ability of a material to conduct heat. When a material has high thermal conductivity, heat transfer occurs at a higher rate. Thermal conductance is the amount of heat that passes through a material of a specific area and thickness. The thermal conductance of a material can be determined when the area, thickness, and thermal conductivity are known. The thermal conductivity of a material is represented by

$$\lambda = \frac{kA}{L}; \quad (2)$$

where λ is the thermal conductance, k is the thermal conductivity, A is the cross-sectional area, and L is the thickness of the material.

Thermal conductivity is affected by a number of factors, including temperature and electrical conductivity. In metals, electrical conductivity decreases with increasing temperature. In this case, thermal conductivity remains constant. In alloys, because there is little change in electrical conductivity, thermal conductivity increases as the temperature increases. In polymers, however, thermal conductivity remains constant at low temperatures. In metals, electrical conductivity tracks thermal conductivity as valence electrons transfer electric current and heat (TA Instruments, 2012). The research laboratory of The American Brass Company determined

the relationship between the thermal and electrical conductivities of copper alloys using a number of experiments. In this study, some of the alloys were in the cast state while others were given precipitation hardening heat treatments. Prior to measuring the conductivities of the samples, they were homogenized by annealing. When the thermal conductivity of a material is plotted against its electrical conductivity at the same temperature, as demonstrated in Figure 1, the results between the alloys are similar.

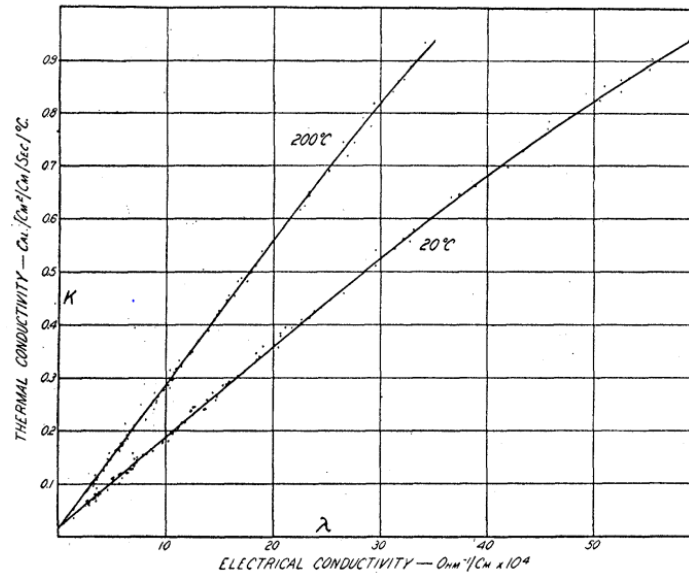


Figure 1. Thermal conductivity plotted against the electrical conductivity (Smith, 1935).

The curve that is plotted is based on the theory that the thermal conductivity is composed of a metallic and nonmetallic part,

$$K = k + c\lambda T, \quad (3)$$

where K is the total thermal conductivity, k is the nonmetallic part, c is the Lorenz ratio for the nonmetallic part, λ is the electrical conductivity, and T is the temperature (Smith, 1935).

Two methods to measure thermal conductivity are steady-state and non-steady-state. Steady-state methods to measure thermal conductivity of a material are performed when the temperature remains constant (Wikimedia Foundation, 2014). Searle's bar method can also be used to measure a material's thermal conductivity. This method involves using a bar of the material being studied and heating it with steam on one side and cooling it with water on the

other side. During this process, the length of the bar is insulated. Once conditions are satisfied, the heat through the bar to the time interval can be calculated using

$$\frac{\Delta Q}{\Delta t} = -\frac{kA\Delta T_{bar}}{L}, \quad (4)$$

where ΔQ is the heat supplied to the bar in time Δt , k is the coefficient of thermal conductivity of the bar, A is the cross-sectional area of the bar, ΔT_{bar} is the temperature difference of both ends of the bar, and L is the length of the bar (Davidson, 1997).

Using non-steady-state methods to measure thermal conductivity in materials allows measurements to be taken quickly. Contrary to steady-state methods, signals are not required to obtain a constant value in non-steady-state methods. Non-steady-state methods often involve the use of needle probes (Wikimedia Foundation, 2014). In experiments, heat flux measurements often make it difficult to measure thermal conductivity. The measurement is absolute when the heat flux is measured directly. When the heat flux is measured indirectly, the measurement is comparative. Because the heat flux of a material has to flow through the sample, the heat losses or gains must be reduced in the radial direction by insulating the material. In most materials, high thermal conductivity results in a high heat flux.

Axial flow methods are the method of choice for measuring a material's thermal conductivity. Main issues that result from using this method are the radial heat losses in the axial heat flow from the electrical heater on one end. As the temperature of the surroundings increases, it becomes more difficult to maintain these losses. An example of the axial flow method for measuring thermal conductivity in a material is the guarded or unguarded heat flow meter method. Using this method, the thermal conductivity is ultimately calculated by

$$k_S = k_R \frac{\frac{\Delta T_1 + \Delta T_2}{2}}{\Delta T_s}, \quad (5)$$

where k_R is the thermal conductivity of the references, ΔT_1 is the temperature change across the reference material connected between the heater and sample, ΔT_s is the temperature change across the sample, ΔT_2 is the temperature change across the second reference sample connected between the bottom side of the sample and the coolant, and k_s is the thermal conductivity of the unknown sample (see Figure 2).

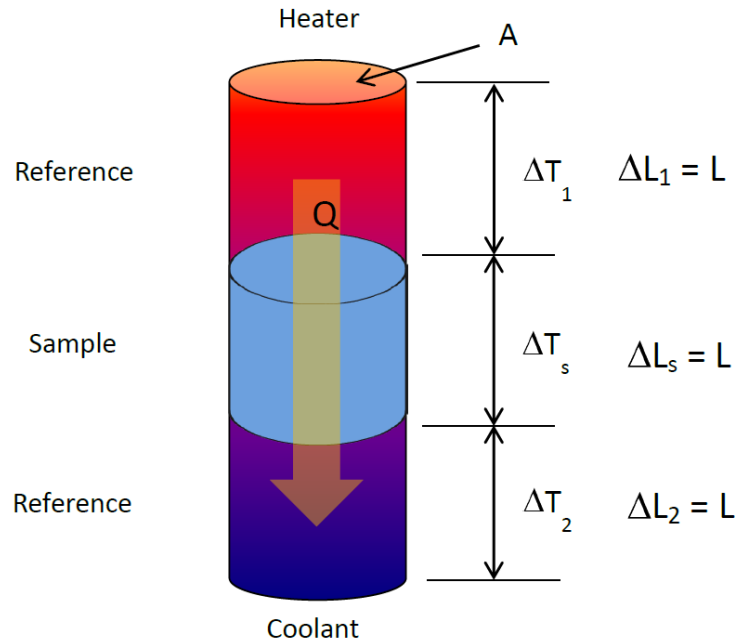


Figure 2. Comparative cut bar set-up method (TA Instruments, 2012).

The guarded or unguarded heat flow meter method involves the use of a flux gauge. Thermocouple plates are located on both sides of the reference plate. These plates are connected to an electrical signal that is proportional to the differential temperature. To ensure that the assembly is durable, it is covered in a protective coating. It is important to ensure that the flux gauges are stable, calibrated, and that they remain unaffected by the thermal cycling (TA Instruments, 2012).

1.3 Literature Review

An experiment conducted by Wang and Lo, 1996 examined the effects of heat treatment on the thermal conductivity of 6061 aluminum matrix composites. In this case, thermal conductivities were taken by the laser-flash method, which measures the thermal diffusivity of the material. This is done by sending a laser or energy pulse to one surface of a sample and measuring the time lapse for energy to reach the second side. The thermal conductivity of the sample was then calculated as the result of the thermal diffusivity, specific heat, and density of the material. In addition to the thermal diffusivity test, a Vickers hardness test was also conducted in attempt to correlate the material structure to the thermal properties.

A second study conducted by Auburn University (Bakhtiyarov, Overfelt, & Teodorescu, 2001) examined the thermal and electrical conductivities of A356 and A319 aluminum alloys. In

this study, the alloys were studied at both solid and liquid states. Electrical conductivity was measured by a rotational contactless inductive measurement apparatus. In this apparatus, the conducting material is rotated in a magnetic field to create currents, which generates an opposing torque, proportional to the electrical conductivity of the material. The thermal conductivity was then calculated using the proportionality of thermal and electrical conductivities, as stated in the Wiedemann-Franz-Lorenz law.

Another setup for measuring thermal conductivity is Searle's bar method. Searle's bar method involves using steam flowing through a tube to heat one end of a sample and cooling the other end using water flowing through a hose. Thermocouples are placed at four points. Two on the sample and one each for the water inlet and outlet.

Figure 3 shows the Searle's bar method apparatus. The heat flowing through the sample can be calculated from the difference between the inlet and outlet temperatures T_3 and T_4 . By using the difference between temperatures T_1 and T_2 along the bar and the dimensions D and d the thermal conductivity of the sample can be calculated.

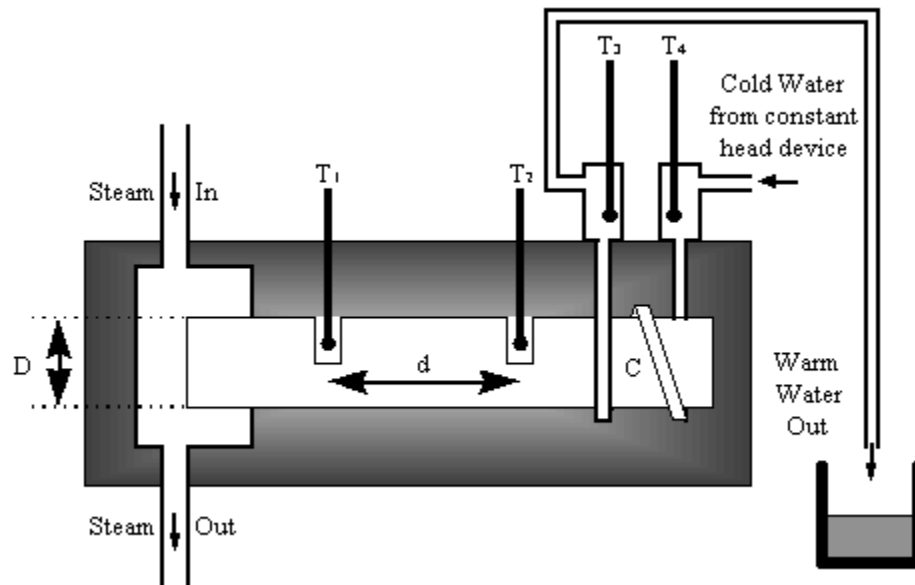


Figure 3. Searle's bar method apparatus for measuring thermal conductivity (*Davidson, 1997*).

In a study that was conducted, the thermal conductivity of polypropylene filled with copper particles was observed. Composite fillers were used because the electrical behavior of the materials is similar to the behavior of the metallic fillers. To estimate the sample's thermal

conductivity, a periodical method was used based on the use of a small temperature modulation in a parallelepiped-shaped sample. The sample was placed between two metallic plates. The first plate is heated periodically using sinusoidal signals and the temperature was measured by placing thermocouples inside of the plates. The thermal conductivity of the sample was calculated using

$$k = b\sqrt{a}, \quad (6)$$

where k is the thermal conductivity, b is the thermal effusivity, and a is the diffusivity (Boudenne, Ibos, Fois, Majesté, & Géhin, 2005).

This method obtained the thermo-physical parameters in one measurement. Based on the investigation, it was concluded that the size of the fillers affects the percolation threshold, which was determined at lower filler concentrations and depends on the interactions between the polymer fillers.

Studies were conducted on the relationship between electrical and thermal conductivities in metals. The Wiedemann-Franz law produces a relationship between the electrical conductivity and thermal conductivity of a metal. This relationship is qualitatively expressed as

$$\frac{\kappa}{\sigma} = LT \quad (7)$$

where, κ is the thermal conductivity in $\frac{W}{m \cdot K}$, σ is electrical conductivity in $\Omega^{-1}m^{-1}$, T is the temperature in K, and L is a proportionality constant equal to $2.45 * 10^{-8} W\Omega K^{-2}$ (Nave, Thermal Conductivity and the Wiedemann-Franz Law, 2000).

The relationship is based on the fact that both thermal transport and electrical transport in metals is based on the movement of free electrons in the metal. Wang et al. studied the Wiedemann-Franz relationship in polycrystalline gold nanofilms from 3 K to 300 K. Their apparatus setup consisted of using the gold nanofilm itself as a Joule heater. The applied power was kept to less than several microwatts in order to minimize the increase in temperature of the gold nanofilm. It was found that at low temperatures

(<40K) the measured Lorenz number increases with decreasing temperature violating the Wiedemann-Franz law (Wang, Liu, Zhang, & Takahashi, 2013).

Woodcraft produced a model for predicting the thermal conductivity of aluminum alloys in the region from the superconducting transition (1 K) to the cryogenic region (4 K) from room temperature measurements. For low temperature measurements of thermal conductivity the Wiedemann-Franz law is used to derive the thermal conductivity of the alloy from their electrical conductivity. At low temperatures, thermal conductivity derived from the electrical conductivity using the Wiedemann-Franz law agrees with the observed value within 10%. For room temperature measurements for Wiedemann-Franz law is not sufficiently accurate to produce an accurate prediction of thermal conductivity from electrical conductivity in aluminum alloys (Woodcraft, 2005).

Chapter 2: Methodology

This section addresses the methodology followed in the project, including the materials selected, the measurement apparatus created and built, and test samples and processing methods used for data acquisition and analysis.

2.1 Materials and Processing

This section details the selection of the aluminum alloys used in this study (Pure Al, wrought 6061, and cast 319 and A356 alloys). 6061 does not exhibit secondary phases, while 319 and A356 have secondary structures which are of great interest for this project. Furthermore, 319 was selected due to the amounts of copper in the material, when compared to the remaining two alloys. Additionally, the higher concentration of magnesium in 6061, but reduced amounts of silicon was to be examined, when compared to the lower magnesium concentrations, but higher silicon concentrations present in 319 and A356. For further details on the compositions of these three alloys, as shown in Table 1.

Table 1. Chemical compositions of aluminum 6061, 319, and A356 alloys

Composition [wt%]										
Material	Al	Cr	Cu	Fe	Mg	Mn	Si	Ti	Zn	Other
6061 (Al-Mg-Si)	95.8-98.6	0.04-0.35	0.15-0.40	<0.70	0.80-1.2	<0.15	0.40-0.80	<0.15	<0.25	<0.15
319 (Al-Si-Cu-Mg)	83.8-91.5	0	3.0-4.0	<1.0	<0.10	<0.50	5.5-6.5	<0.25	<3.0	<0.50
A356 (Al-Si-Mg)	91.1-93.2	0	<0.20	<0.15	0.30-0.45	<0.10	6.5-7.5	<0.20	<0.10	<0.15

The three materials under consideration are all aluminum-silicon alloys. 6061 has the lowest concentration of silicon, followed by 319, and finally by A356 (all hypo-eutectic alloys). The Al-Si phase diagram and the study alloys can be seen in Figure 4.

Aluminum 6061 features a pancake grain structure (primary α -Al), and a Mg-Si strengthening precipitate system. Aluminum 319 has both primary and secondary structures - an α -Al matrix and eutectic phase, including secondary eutectic Si particles of different morphology. Since 319 can have at least nine different elements in measurable quantities there are a great variety of phases which may chemically form; this alloy has an Al-Cu precipitate strengthening system, in contrast with the Mg-Si system in 6061. Finally, A356 has a similar structure with 319 (α -Al matrix and eutectic phases), however having the same strengthening precipitate system as 6061.

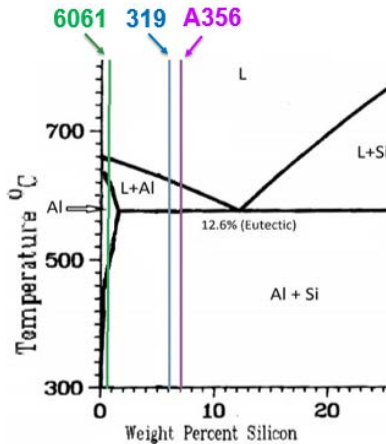


Figure 4. Al-Si phase diagram showing the Si compositions of 6061, 319, and A356 alloys.

The alloys, widely used in the aerospace and automotive industry, have been extensively studied for their mechanical properties, as seen in Table 2.

Table 2. Important properties of aluminum alloys

Material	Density [kg/m ³]	Modulus of Elasticity [GPa]	Thermal Conductivity [W/(m·K)]	Specific Heat Capacity [J/(g·K)]
Pure Aluminum	2700	68.9	237	0.90
6061	2700	68.9	170	0.90
319	2796	74.0	110	0.96
A356	2713	72.0	167	0.96

The two main classes of aluminum selected for this experiment were wrought and cast. Wrought alloys exhibit a low silicon content and tend to be grain size dominated (as seen in Figure 5). Cast aluminum alloys however, possessing higher silicon content, create dendrite networks within the α -Al regions, as well as eutectic Si particles, which greatly impact the thermo-physical properties of the material.

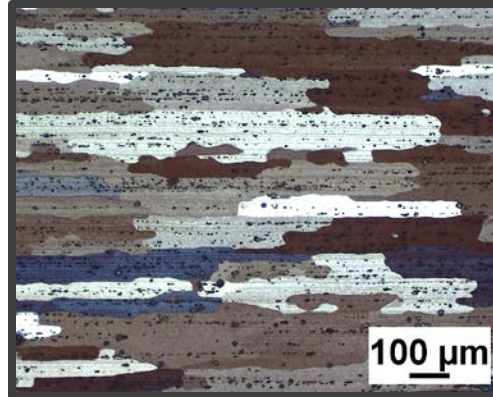


Figure 5. Optical micrograph showing elongated grain and grain boundaries in rolled 6061.

During the solidification of metal alloys, a number of microstructures may form, of different chemical compositions and structures within the overall alloy. The exact nature of these microstructures is a consequence of the thermal history, the processing (if any) of the material, and the overall chemical composition of the alloy. Of the many microstructural features that form, one type, dendrites, shown in Figure 6, will now be explored at a greater detail.



Figure 6. An image of dendrites (Pace Technologies, 2014).

Dendrites result from the geometric growth of metal crystals within a cooling alloy. These crystals have a tendency to grow with specific orientations, creating multidirectional branches, and resembling a type of fractal growth, or rather a tree (Collaboration for Nondestructive Testing Education, 2012). The large central branches are called as primary branches, with secondary branches offshoots of the primary, and tertiary off shooting from the secondary, and so forth. In a given alloy, multiple dendrites may grow within the solidifying alloy, eventually suppressing each other's growth as shown in Figure 7.

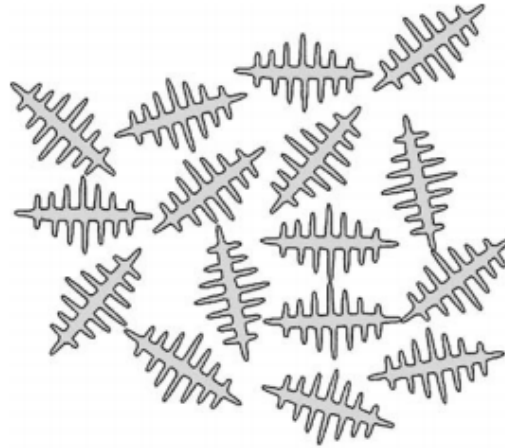


Figure 7. Theoretical dendrite growth pattern (Malekan & Shabestari, 2009).

While there are many ways to characterize dendrites, the most common quantities used to describe them are the arm spacing, cell interval, and cell size. Arm spacing refers to the distance between branches (arms) within the dendrite. This would be further described as secondary, tertiary, and so forth. Hence secondary dendrite arm spacing would refer to the distance between adjacent secondary branches. The cell interval of a dendrite refers to the distance between adjacent dendrite cells, essentially the spacing between primary dendrite branches on adjacent dendrites. Finally, dendrite cell size refers to the characteristic size of a single dendrite cell, typically expressed as the width of the dendrite, but may be characterized with other physical measurements in certain cases (Kaufman & Rooy, 2004).

All three of these properties are closely related to the solidification rate and the chemical composition of the specific alloy. In fact, one model, presented by Kurz & Fisher in 1984, and again by Xu & Liu 2005, attempts to predict arm spacing using the equation

$$\lambda_2 = \sqrt[3]{166 \times \frac{\Gamma D_d \ln\left(\frac{C_{eut}}{C_o}\right)}{m(1-P)(C_o - C_{eut})} \times t_f} \quad (8)$$

where λ_2 represents the secondary dendrite arm spacing, Γ represents the Gibbs-Thomson coefficient, D_d represents the diffusion coefficient, C_{eut} represents the eutectic composition weight percentage, C_o represents the initial composition weight percentage, m represents the slope of the liquidus, P represents the partition coefficient, and t_f represents the local

solidification time (Rao, Tagore, & Janardhana, 2010). This modeling attempts to model the known relationships between dendrite size, spacing, content and diameter (see Figure 8).

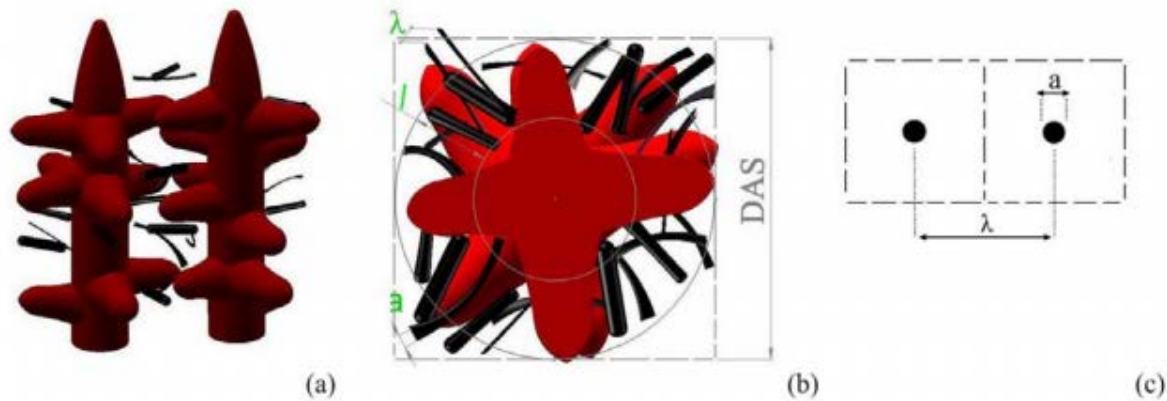


Figure 8. Diagram showing the length that describe the morphology of primary dendrites (a) the relationship between the primary dendrite size and the average length of the silicon phase (b), and the relationship between spacing and diameter of silicon (c) (Shabani, Mazahery, Bahmani, Davami, & Varahram, 2010).

Of all these parameters, a majority of the terms are based upon the material itself, and remain independent of processing or cooling. The Gibbs-Thomson coefficient relates to the geometric shape, the solid-liquid system, and the interfacial energy, all related to the chemical composition (Gibbs-Thomson equation, 2004). The diffusion coefficient relates to the diffusion between two or more species or molecules – again an intrinsic value. Both composition values are a consequence of the chemical composition of the specific alloy as well, while the slope of liquidus is again a material property. The partition coefficient represents the concentration of two different phases of a single compound, which may be taken from an appropriate phase diagram. The only term related to the processing is therefore the local solidification time, that is how fast or slow the alloy cools. This relationship may be seen in Figure 9.

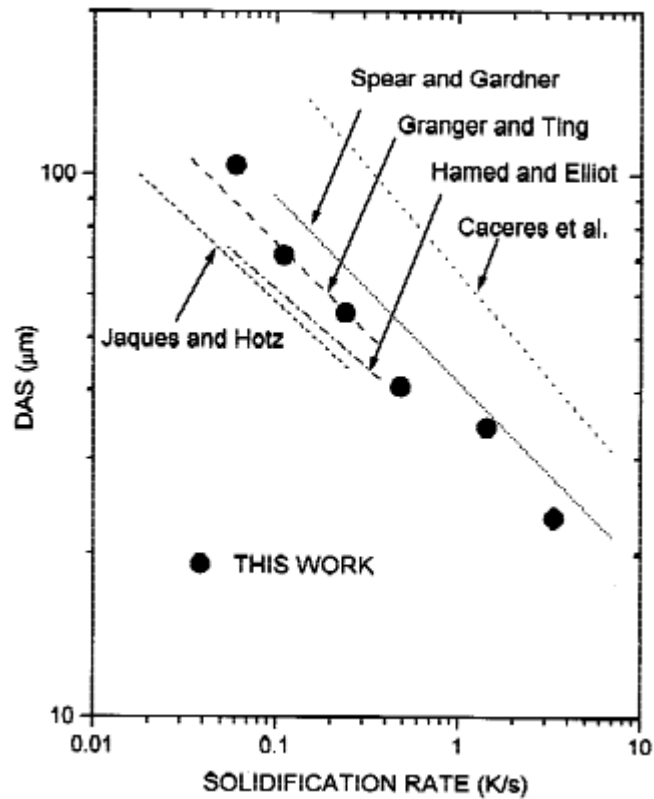


Figure 9. Solidification rate vs. secondary dendrite arm spacing (Vazquez-Lopez, 1999).

A second model used to predict secondary dendrite arm spacing,

$$\lambda_2 = 7.5 \times t_f^{0.39}. \quad (9)$$

This relationship first reported in 1950, and later confirmed by additional experiments, supports the dependence between solidification time (t_f) and secondary dendrite arm spacing (λ_2). However, the alloy under question for this model was a binary copper-aluminum alloy, rather than the aluminum-silicon alloys considered in equation (9). The power attached to the solidification time has change from 0.33 to 0.39, while the constant term, as mentioned in the above paragraph, remains a function of the material itself under question (Davis, 1993).

In aluminum alloys, the silicon particle morphology can be controlled through strontium additions. Small quantities of strontium are added to the alloy to change the morphology of silicon crystals to a fibrous form. The modification of 319 and A356 alloys results in a change in thermal conductivity, as investigated in our experiment.

The largest phase generally found in 319 save pure aluminum is eutectic silicon. As seen in it may take the shape of thin parallel sheets, which depending on the presence of strontium may take a cluster appearance (Lombardi, Elia, Ravindran, Murty, & MacKay, 2011). The longer the precipitate is heated for, the longer this phase may grow, while at the same time processing methods may alter the form and size of this eutectic phase.

For A356 the microstructure is characterized by a primary phase α -Al with the presence of dendrites and an eutectic mixture of aluminum and silicon, the precipitation of Mg_2Si , the precipitation of the eutectic and the end of solidification.

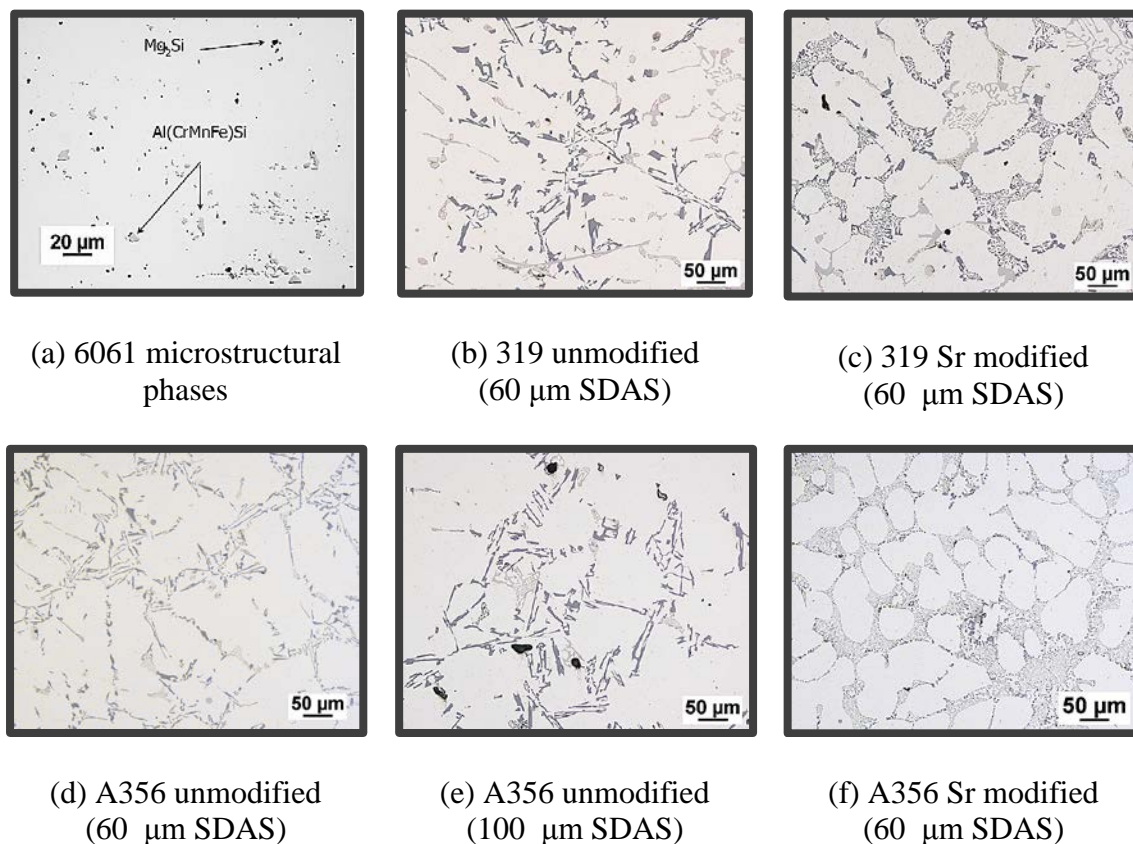


Figure 10. Microstructures of studied 6061, 319, and A356 alloys.

The particle size and shape factor of the secondary Si eutectic particles were measured by examining the optical micrographs images and measuring the size and shape factor of all

particles in the image. The particle diameter refers to the equivalent circular diameter of the particle.

The graphs below show the size of the particle and the frequency at which the particle size was observed. The particle size and shape factor was found by producing a weighted average of the particle sizes and shape factors observed with regards to the frequency observed.

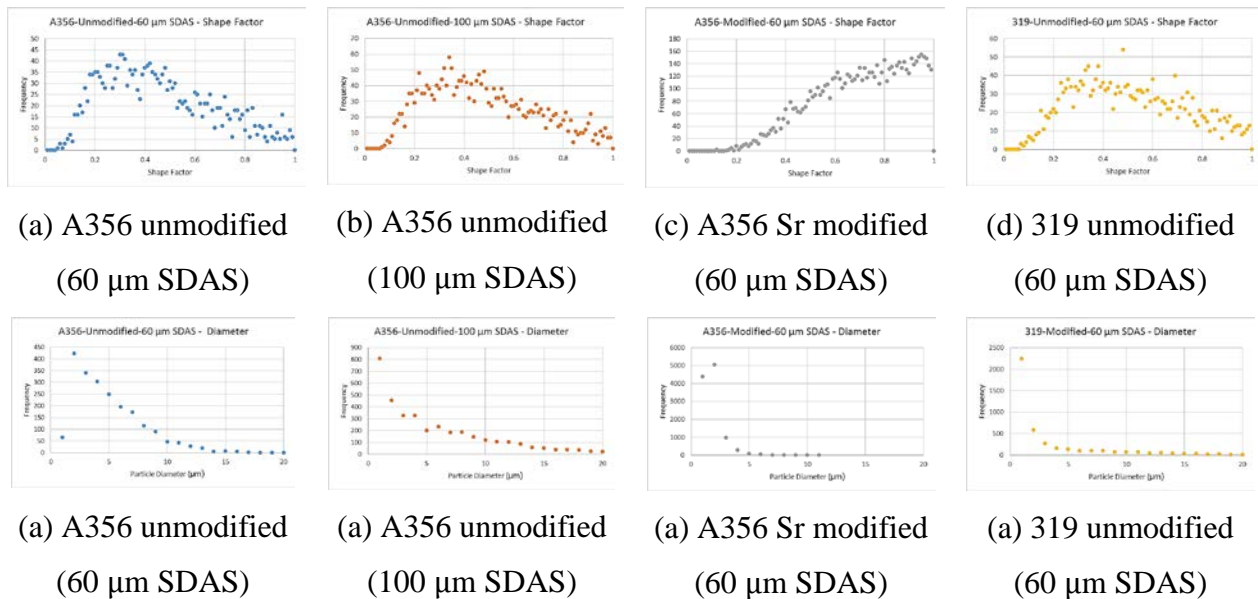


Figure 11. Top row: shape factor; bottom row: particle diameter (for 319 and A356 alloys).

2.2 Heat Treatment and Precipitation Strengthening

The selected alloy samples were solution heat treated in order to make their starting state identical. The 6061 samples were reused from a previous project and had already been previously artificially aged. They were solution heat treated in order to dissolve the precipitates formed from artificial aging and return the samples to their initial state. The 319 and A356 samples were heat treated in order to ensure that factors affecting precipitate size in casting were eliminated, ensuring uniformity amongst the samples.

The 6061 and A356 alloy samples were solution heat treated at 540 °C for 4 hours and the 319 alloy samples were solution heat treated at 500 °C for 4 hours. The alloys were rapidly quenched in boiling water in order to ensure that the precipitates remained in their solutionized form when they returned to room temperature. All alloy samples were naturally aged for 24

hours at room temperature. From the 6061 samples, 4 samples were selected to be artificially aged. One sample each was artificially aged for 1.5 hours, 4 hours, 8 hours, and 16 hours. No 319 and A356 samples were artificially aged. Table 3 shows the solution heat treatment and artificial aging conducted.

Table 3. Table of solution heat treatment and artificial aging

Alloy	Solution Heat Treatment		Artificial Aging	
	Temperature (°C)	Time (hours)	Temperature (°C)	Time (hours)
6061	540	4	180	1.5, 4, 8, 16
319	500	4	N/A	N/A
A356	540	4	N/A	N/A

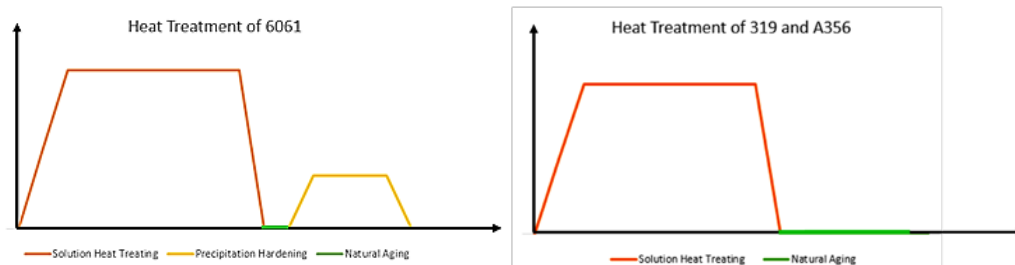


Figure 12. Heat treatment procedures for 6061, 319, and A356.

The heat treatment procedure for 6061 is shown in Figure 12. The samples are first solution heat treated at 540°C and then quenched in boiling water. Then the samples were left to naturally age for 24 hours before four were taken for further artificial aging. The last 6061 sample was left untreated. The heat treatment procedures for 319 and A356 followed a similar procedure as that shown in Figure 12 minus the artificial aging.

The artificial aging of 6061 results in the growth of the Si precipitates in the α -Al matrix. Figure 13 shows the strength of 6061 and precipitate growth in the α -Al matrix as a function of aging time. As aging time increases the strength of 6061 increases until it hits a peak at T6 condition before what is known as overaging sets in where the precipitates become large and their strengthening effect is considerably reduced.

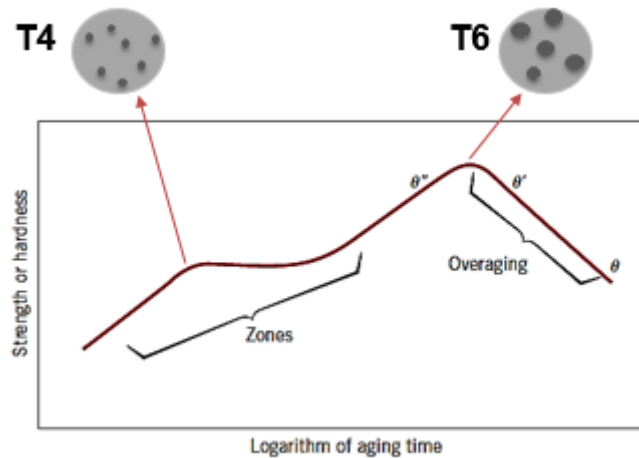


Figure 13. Strength and precipitate growth of aluminum 6061 with regards to aging time.

Precipitation strengthening or precipitation hardening is a technique to increase the yield strength of malleable metals such as aluminum. Precipitation strengthening increases the strength of the metal alloy by forming extremely small and uniformly dispersed second-phase particles within the original phase matrix. These particles act to impede dislocation movement, thereby strengthening the alloys

For an alloy to be able to be precipitation strengthened there must be a terminal solid solution with a decreasing solubility as temperature decreases. Typically the alloy is first heated above the solvus temperature until a homogeneous solid solution is formed. Then the alloy is rapidly cooled in a process called quenching. Quenching forms a supersaturated solid solution which is not an equilibrium structure. The atoms do not have time to diffuse to potential nucleation sites and thus precipitation does not occur. The final step is aging where the supersaturated solid solution is heated below the solvus temperature to form a finely dispersed precipitate (Key to Metals AG, 2010).

During the aging process for aluminum alloys, the precipitates grow in size. The effect of precipitate size on electrical and thermal conductivity has not been studied extensively. However, a general relationship between precipitate size and electrical and thermal conductivity can be determined by examining the electrical and thermal conductivities of an aluminum alloy at various temps. In the alloys studied, there are two types of strengthening precipitate systems: Mg-Si (in 6061 and A356 alloys) and Al-Cu and Al-Cu-Mg-Si (in 319 alloy), which allows a comparison and understanding of the additional contributions of Cu on the thermal properties of these alloys.

2.3 Literature Review Relevant to the Relationships between Transport Properties and Materials Microstructures

In considering conductive properties, a study featured in the Journal of Materials Research explored the relationship between thermal conductivity and two dendrite properties – secondary spacing and the integral dendrite perimeter. The integral dendrite perimeter is a function of the cell size and to a certain extent dendrite spacing – both contributing to the overall perimeter of the dendrite cell. This journal experimentally found that as the secondary dendrite arm spacing increased, the thermal conductivity decreased (Figure 14). Similarly, as the perimeter increased, the conductivity was found to increase, as shown in Figure 15 (Vazquez-Lopez, 1999). However, currently, these models use empirically generated equations, rather than being defined by the properties of the individual system.

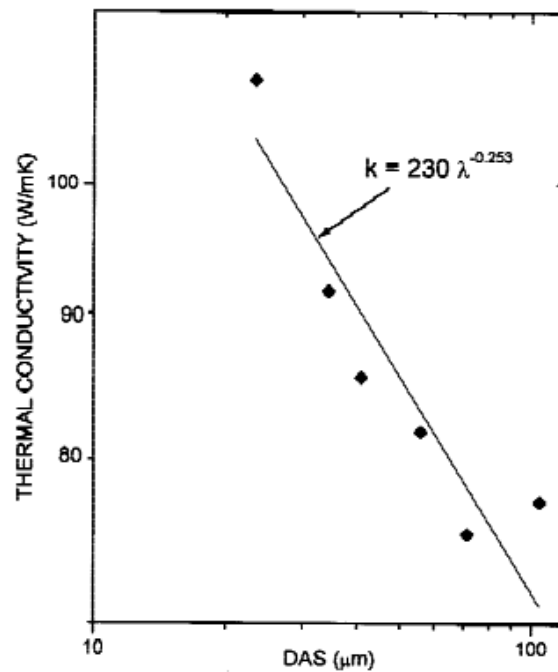


Figure 14. Dendrite arm spacing vs. thermal conductivity in Al cast A319 (Vazquez-Lopez, 1999).

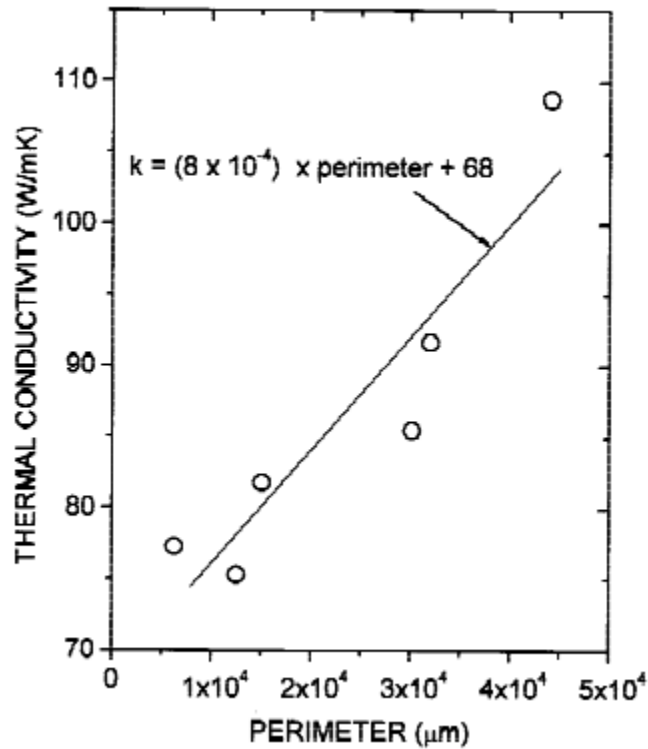


Figure 15. Dendrite perimeter vs. thermal conductivity in Al cast A319 (Vazquez-Lopez, 1999).

Much like the effect of the dendrite properties on thermal conductivity, dendrites also effect the electrical properties of the alloy. Figure 16 shows that as the cooling rate increases, the electrical resistivity increases, and thus the conductivity (the reciprocal of resistivity) decreases. As was mentioned above, as the cooling rate increases, dendrite cells remain smaller in terms of size and secondary dendrite spacing. Thus, dendrite properties affect both electrical and thermal transport within the alloy itself (Grandfield & Eskin, 2013).

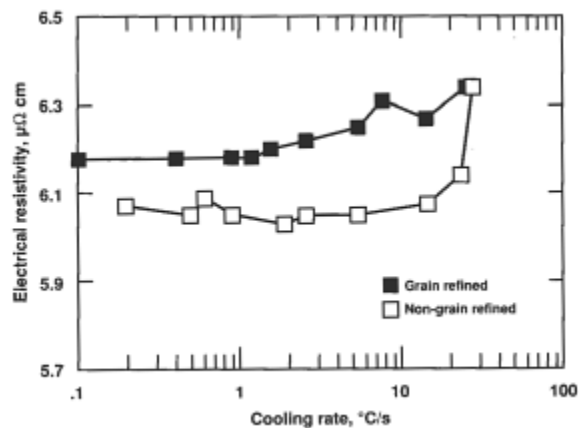


Figure 16. The effect of cooling rate on electrical resistivity (Grandfield & Eskin, 2013).

Based on research, heat treatment and aging time in aluminum alloy samples affect their thermal and electrical conductivities. Research has been conducted to investigate these effects.

The research conducted involved observing the effects of heat treatment on the thermal conductivity of 6061 Al alloy samples in the T6 condition. To determine these effects, micro-hardness tests were conducted after heat treating the samples. Samples were cut, polished, and solutionized at 543°C for 2 hours in a purified argon atmosphere. The samples were then quenched in cold water. This was followed by aging the samples at 163°C for different amounts of time and quenched again before conducting micro-hardness tests. In this experiment, the thermal conductivity was calculated as a product of the measured thermal diffusivity and specific heat of the samples. It was shown that an increase in aging time resulted in an increase in thermal diffusivity. Aging also caused an increase in the specific heat of the samples. At the initial stage of aging, there was a decrease in the electrical conductivity. Results showed that there is positive aging time dependence, as shown in Figure 17 (Wang, H, et al., 1996).

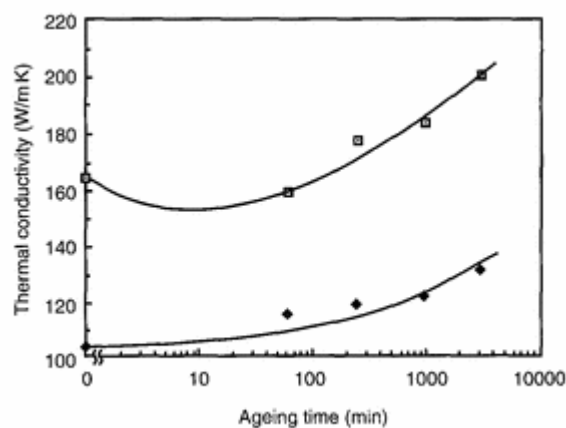


Figure 17. Thermal conductivity of Al 6061 and SiC_p/6061 Al composite measured as a function of aging time (Hernandez-Paz, 2003).

In other research, the effects of T5 and T6 heat treatments on the mechanical properties of 319 alloys were studied. The effects were correlated to the mechanical behavior as well as

their microstructure. Samples measured at a length of 196 mm were solutionized and aged. The samples were solutionized for approximately 4 hours at a temperature of 500°C and quenched. The samples were then aged at 170°C, 200°C, and 220°C. Rockwell hardness tests were performed on the samples and conductivity measurements were done using a Foster probe on the sample surfaces. It was found that the electrical conductivity reaches steady state after 4 hours of treatment. This indicates that there are no more atoms in the solid solution and that the hardening mechanism is no longer effective in this case. As seen in figure 2, there are no differences in the peak values of the T5 condition when looking at the hardness results and comparing it to the T6 condition. A smaller amount of solid solution atoms available for the T5 condition results in a leveling off of the electrical conductivity after a short period of time in comparison to the T6 condition. Figure 2 shows the effects of aging on these values.

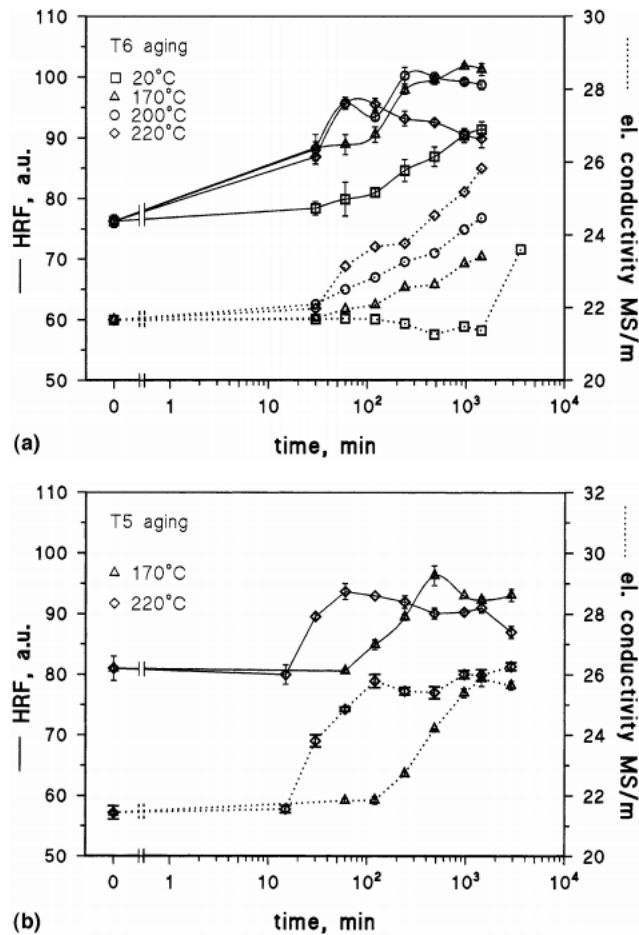


Figure 18. Electrical conductivity and hardness values of artificially and naturally-aged samples in (a) T6 and (b) T5 conditions (Cerri, E., et al., 2000).

Based on the experiment, it was concluded that the fracture of the samples in the different solution treatments developed similarly. It was observed that Si particles break in the direction perpendicular to the tensile axes. In the heat treated samples, the cracks were present (Cerri, E., et al., 2000).

Previous research has studied the effects of aging and heat treatment in A356 aluminum alloys. In this study, these effects were investigated by measuring the impact strength, hardness, and tensile testing. Samples were prepared by polishing and etching them. The microstructures of the samples were analyzed using a metallurgical microscope. An impact testing machine was

used as well as a Vickers hardness tester. These tests were performed on samples that underwent heat treatment and on samples that were in as-cast condition. As shown in figure 3, results revealed that as the section size is reduced, the impact strength increases for the samples in as-cast condition. The impact strength for the samples that underwent heat treatment and aging improved in comparison to the as-cast condition. This is a result of the higher grain refinement in the heat treated and aged condition.

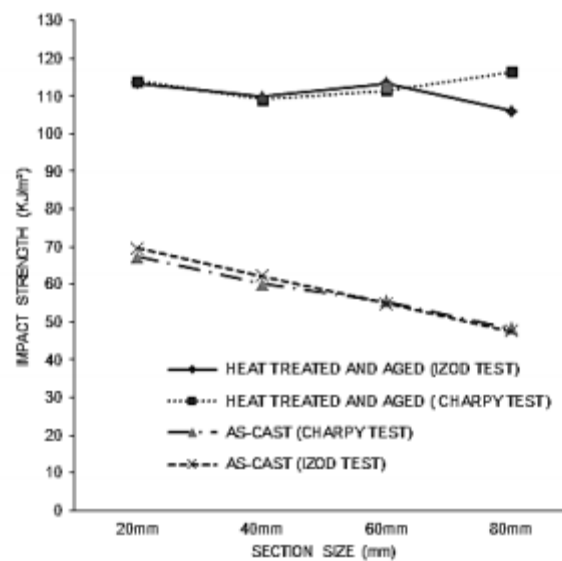


Figure 19. Variation in impact strength with section size (Akhil, K., et al., 2014).

When evaluating the measurements from the hardness tests, it is shown that as the section size decreases, the micro-hardness of as-cast samples increases. The hardness of the heat treated and aged samples were improved but remains constant with variation in section size, as indicated in Figure 19.

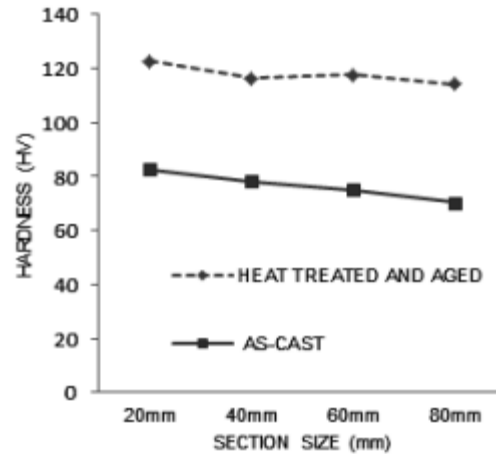
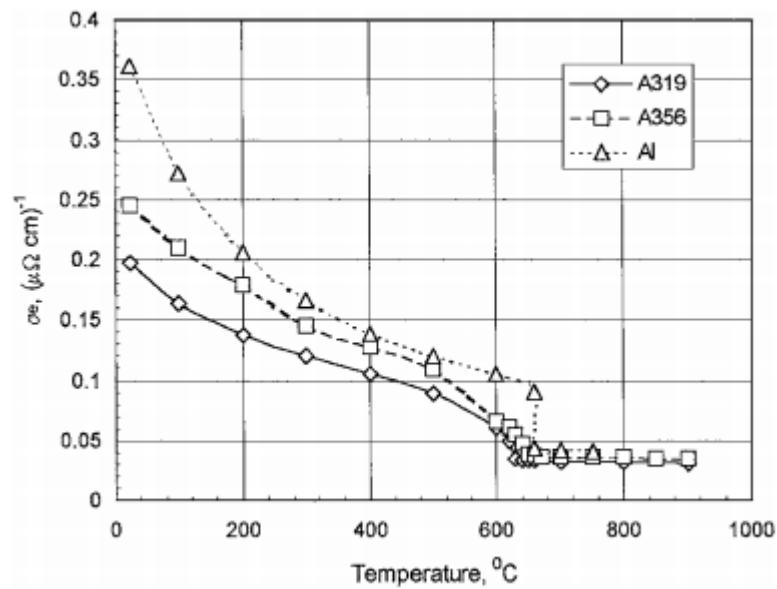


Figure 20. Variation in hardness with section size (Akhil, K., et al., 2014).

Based on the research, it was concluded that the hardness values increased with decreasing section size from 80 mm to 20 mm because of the grain refinement. When the samples are heat treated and aged, the mechanical properties such as the impact strength and hardness are improved (Akhil, K., et al., 2014).

A study was conducted to present the electrical conductivity for pure aluminum, A356 and A319 cast Al alloys using a rotational technique (Bakhtiyarov, S. I., et al., 2001). In this experiment, the electrical resistivity of the samples was measured at high temperature using an apparatus. A rheometer provided rotational speed for the apparatus while a thermometer inserted in the assembly was used to determine the temperature of the samples. An infrared thermometer output was calibrated by comparing against thermocouple data. Figure 21 shows the variation of electrical conductivity and thermal conductivity with temperature for the pure aluminum, A319, and A356 samples.

(a)



(b)

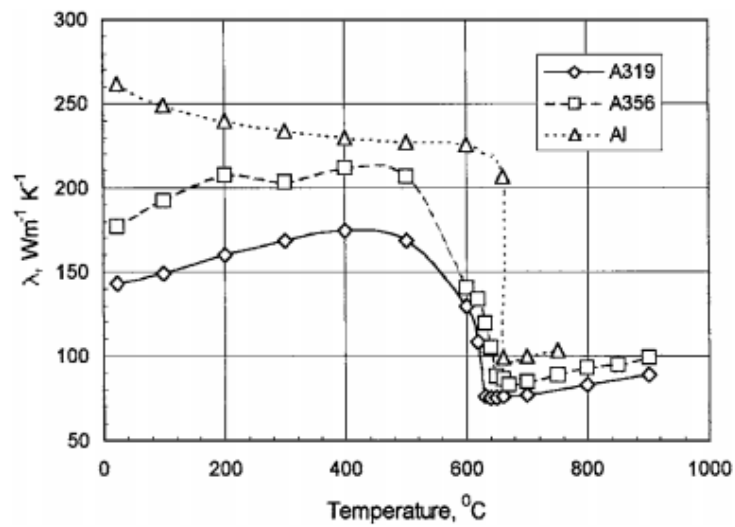


Figure 21. Variation of (a) electrical conductivity and (b) thermal conductivity with temperature for pure aluminum, 319, and A356 (Bakhtiyarov, S. I., et al., 2001).

Other research has been conducted to study the effects of heat treatment and aging on modified and unmodified A356 samples. Based on the experiment, it was found that modified alloys demonstrated a higher electrical conductivity in the as-cast condition than the unmodified alloy. This is caused by the movement of electrons. Electrons flow more easily through the finer eutectic silicon in the modified alloy than in the coarse silicon present in modified alloys. The change in electrical conductivity of the unmodified alloy that has undergone heat treatment is larger than the modified alloy. This is a result of the morphology changes. Larger morphology changes take place in the unmodified eutectic silicon than in the modified, causing larger changes in electrical conductivity. The electrical conductivity in T4 condition of A356 samples with unmodified and Sr-modified eutectic Si morphology are shown in Figure 22.

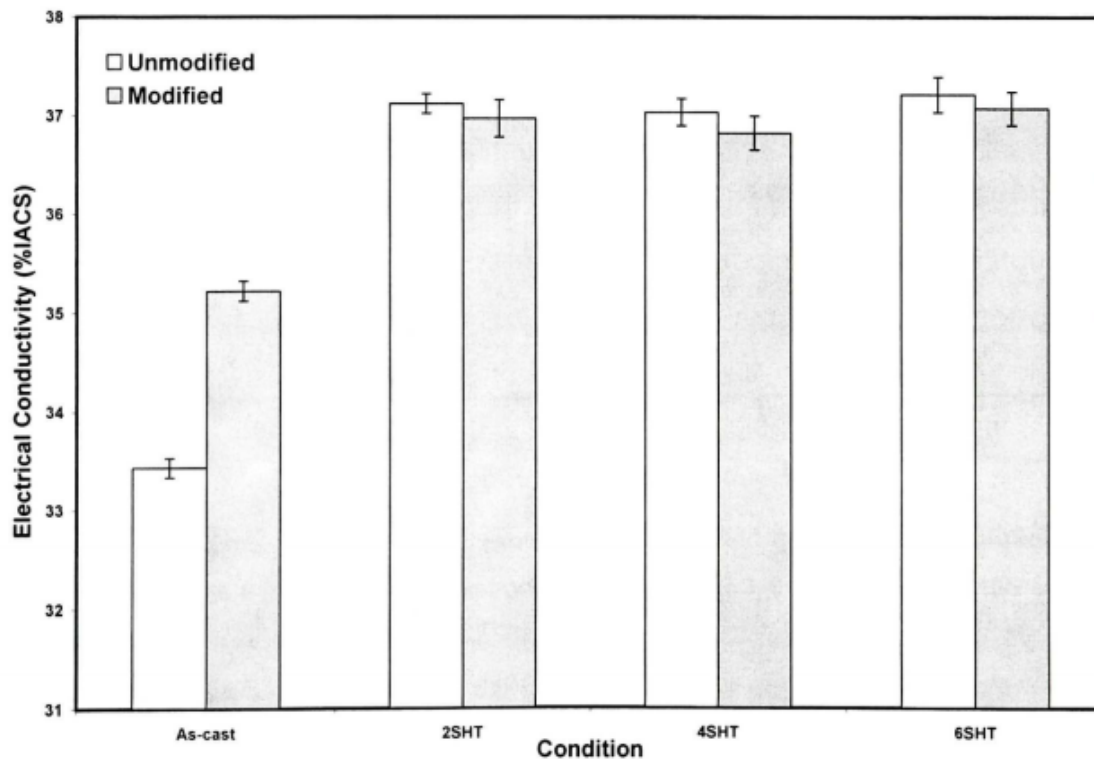


Figure 22. Electrical conductivity at T4 condition of unmodified and modified A356 coupons upon solution treatment at 540°C (Hernandez, Paz J., 2003).

In the same research, it was shown that solution heat treatment times had an effect on the matrix of the micro-hardness. As shown in Figure 22, as the time for heat treatment increased, the micro-hardness values in the T6 condition decrease. This is caused by the small vacancy clusters, which are formed as solution heat treatment proceeds, resulting in a reduction in the number of possible nuclei for further precipitation (Hernandez, Paz J., 2003).

Additional research has shown that adding Sr to an Al-Si melt increases the electrical conductivity of the resulting cast. This was attributed to the fact that in the modified condition the fibers impede electron flow less than the plate in the unmodified condition (Manzano-Ramirez, Nava-Vazquez, & Gonzalez-Hernandez, 1993).

Table 4. Density and electrical conductivity with regards to Sr content (Manzano-Ramirez, Nava-Vazquez, & Gonzalez-Hernandez, 1993)

Sample Number	ρ (g/cc)	Pct IACS	Pct Sr
1-5	2.420	24.8	0.0122
2-5	2.480	24.2	0.0080
3-5	2.435	24.3	0.0062
4-5	2.516	25.5	0.0063
5-5	2.193	fail	0.0128
1-2	2.357	23.8	0.0134
2-2	2.450	25.1	0.0165
3-2	2.477	fail	0.0066
4-2	2.462	25.2	0.0131
5-2	2.457	25.1	0.0086

Table 5. Density and electrical conductivity of unmodified Al-Si melts (Manzano-Ramirez, Nava-Vazquez, & Gonzalez-Hernandez, 1993)

Sample Number	ρ (g/cc)	Pct IACS	Pct Sr
1-1'	2.207	19.73	0.0007
2-1'	2.436	22.50	—
3-1'	2.087	21.20	0.0010
4-1'	2.493	22.33	—
5-1'	2.104	19.55	—
1-1	2.255	22.07	—
2-1	2.324	22.50	—
3-1	2.405	20.67	—
4-1	2.412	fail	—
5-1	2.356	21.05	—

Vazquez-Lopez et al. found that thermal conductivity decreased with increasing secondary dendrite arm spacing (SDAS) in Al 319. The decrease was attributed to the fact that the dendrite arm spacing determines the form of the aluminum channels (Vazquez-Lopez, 1999).

2.4 Apparatus: Design and Fabrication

In order to correlate thermal conductivity with microstructural properties, a means of measuring thermal conductivity had to be selected, and in this case, a custom apparatus was designed. This apparatus essentially used a method similar to the one described in Section 1.3 (Boudenne, Ibos, Fois, Majesté, & Géhin, 2005). It relied on measuring a temperature change across a material based on the power applied to a heater at one end of the specimen, as schematically shown in Figure 23.

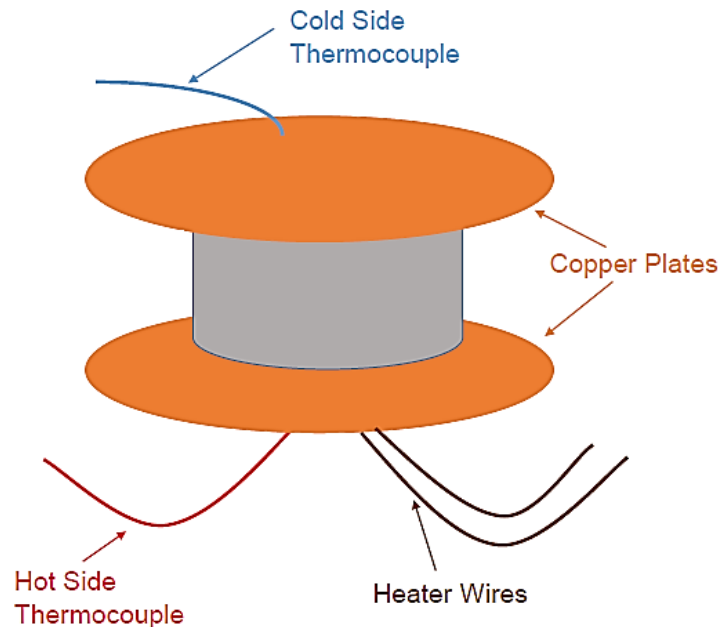


Figure 23. Schematic design of the thermal conductivity measurement apparatus.

The thermal conductivity apparatus was constructed with two copper plates, three sets of Class J thermocouple wires, a heater, a National Instruments DAQ box, and a Keithley 2304A High Speed Power Supply. The two copper plates have a diameter of 3.0 cm and a thickness of 0.5 mm. These plates are polished using Dremmel tool using a 240 rating sand paper. Once the copper plates were cleaned and prepared, a thin layer of 5 minute epoxy was applied to the back face of one of the copper plates. Once dried, a thermocouple was attached to the back of the plate. The purpose of the epoxy was to prevent any electrical connection from occurring between the thermocouple and the plate. The second plate (which would become known as the bottom/heater plate) was then prepared. First, the heater was attached to the back of the plate, and epoxy was used to keep the heater flush and physically connected to the plate. Again, once the epoxy was dried, another thermocouple was physically (but not electrically) connected to the back face of this plate. Each of the two sets of thermocouple wires which had been connected were then connected to the temperature recorder. Similarly, the heater wires are connected to the power controller. A third thermocouple was then connected to temperature controller, intended to measure the ambient temperature of the room. The bottom plate was then epoxied to a bottom stand, with holes cut for the wires (see Figure 24). Once dried, this would serve as the stand for

the sample. Finally, once the setup is complete, the temperature recorder is connected to a computer with the aid of a DAQ box, which then serves as the input for a LabVIEW File, which records temperature readings for each of the three thermocouples in addition to the time each reading was taken as well. This was programmed to record five hundred sets of readings at an interval of 0.5 seconds between readings for all thermocouples simultaneously.



(a) Outside view

(b) Inside of chamber

(c) Connection to electronics

Figure 24. Images of the apparatus and electronics used for thermal conductivity measurements.

In order to reduce the heat loss through the thermocouple wires, and increase the reliability of the measurements of the thermocouple wires, wires were kept continuous and preferably shorter. A minimal and equal amount of wire was exposed to connect the wires to the recorder.

The second apparatus used was a device to assist in measuring the electrical conductivity of samples. This was a Keithly 2002 Digital Multimeter. The two sets of electrical wires featured alligator clips at one end. These clips each held a thin sheet of metal. The resulting output of this is a resistance reading through the wires, clips, and sample (total resistance).

2.5 Test Specimen Geometry

Sample geometry played a significant role in the measurements. Initially we started using cylindrical samples in order to simplify calculations. The samples were machined to a length 52 mm and a diameter of 15.5 mm. After the first set of measurements was done, data analysis

revealed that longer samples experienced a significant heat loss that would affect the final calculations of the thermal conductivities. This observation led the team to decide on a new set of dimensions for the samples. We then machined three different lengths of pure aluminum to use them a baseline for the rest of the measurements. The lengths chosen were 25.4, 12.7 and 6.35 mm (see Figure 25). Measurements were conducted with all three sizes and the more accurate data were obtained using the shortest specimen of 6.35 mm. The heat leak for this sample size was very small and this dimension still allowed the program to detect a difference in temperature needed for our calculations. The rest of the alloys were machined to match the desired dimensions as shown in Table 6. All specimens were machined using the same ESPRIT file specifications. The specimen were all grinded using a 200, 400, 600, 1200 grit paper sequence and a 1.0 micron polishing disk. It is also important to note that both the thermal and electrical measurements were conducted at room temperature.

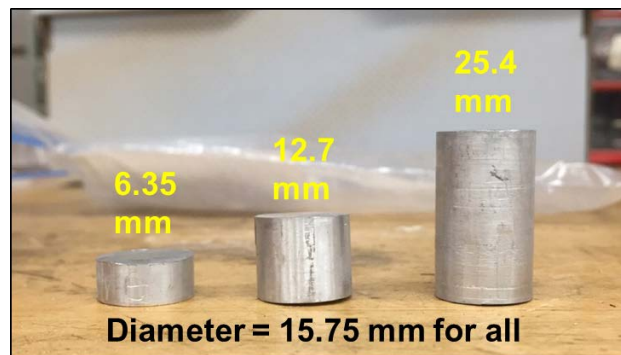


Figure 25. Dimensions of the three pure aluminum test samples.

A total of 18 samples of Pure Al and Al alloys were measured. Five samples of 6061, six samples of 319, and six samples of A356 were prepared. The 6061 samples had a grain size of $550\ \mu\text{m} \times 50\ \mu\text{m}$. Five samples of 319 were unmodified (plate-like eutectic Si morphology) and one sample was modified with Sr additions (finer and rounder eutectic Si morphology). All 319 samples had an SDAS of $60\ \mu\text{m}$. Two samples of A356 were modified with Sr and four samples of A356 remained with unmodified eutectic Si morphology. The Sr modified samples of A356 had $60\ \mu\text{m}$ SDAS. Of the unmodified A356 samples two had $60\ \mu\text{m}$ SDAS and two had $100\ \mu\text{m}$ SDAS. Table 6 displays the samples, their dimensions, and their Sr modification status and SDAS size.

Table 6. Test sample characteristics

Material	Length (mm)	Diameter (mm)	Sr modification	SDAS (μm)
Pure Aluminum	6.90	15.64	n/a	n/a
6061 Naturally Aged (T4)	6.38	15.53	No	60
6061 (Artificial Age, 1.5 hrs)	6.53	15.53	No	60
6061 (Artificial Age, 4 hrs)	7.05	15.52	No	60
6061 (Artificial Age, 8 hrs)	6.83	15.51	No	60
6061 (Artificial Age, 16 hrs)	6.68	15.54	No	60
319 Sr Modified	6.47	15.55	No	60
319 (60 μm) Unmodified	6.79	15.54	No	60
319 (60 μm) Unmodified	7.14	15.54	No	60
319 (60 μm) Unmodified	6.73	15.55	No	60
319 (60 μm) Unmodified	7.03	15.52	No	60
319 (60 μm) Unmodified	6.66	15.52	Yes	60
356 (60 μm) Sr Modified	6.88	15.54	Yes	60
356 (60 μm) Unmodified	6.48	15.49	No	60
356 (100 μm) Unmodified	6.95	15.52	No	100
356 (60 μm) Unmodified	6.78	15.50	No	60
356 (100 μm) Unmodified	6.76	15.51	No	100
356 (60 μm) Sr Modified	6.65	15.51	Yes	60

Chapter 3: Measuring Methods

3.1 Transport Equations

This section shall consider the methodology to turn the measurements and raw data into the results which shall be considered in the results section.

3.1.1 Thermal Conductivity Equations

When the temperature recorder is used, the result is an output file containing five hundred sets of data, taken at 0.5 second intervals over a time period of 250 seconds. Each set of data contains a time stamp and temperatures for each of the three thermocouple wires. The wire connected to the top of the plate shall be called the cold temperature (T_S measured in Kelvin), the thermocouple connected to the lower plate with the heater attached shall be called the hot temperature (T_C measured in Kelvin), and the third thermocouple measuring the ambient temperature shall be called the room temperature (T_R measured in Kelvin).

It is known that

$$R_t = \frac{L}{kA} \quad (10)$$

where, R_t is the thermal resistance of the sample (in Kelvin per watt), k is the thermal conductivity of the sample (in watts per meter-Kelvin), L is the length of the sample (in meters), and A is the cross sectional area of the sample (in square meters). Thus this equation may be rearranged to solve for conductivity, such that

$$\kappa = \frac{L}{R_t A} \quad (11)$$

Using a digital caliper, the length of the sample may be measured directly. Similarly the diameter of the sample may also be measured. Though the samples were machined to be the same size, both the length and diameter were measured three times, with the diameter measured at the, middle, and end of the sample. The average was then computed and used as the effective length and diameter. Using the diameter, the cross sectional area may be calculated by

$$A = \frac{\pi D^2}{4} \quad (12)$$

where, D is the average diameter of the sample (in meters). Thus in order to solve for the conductivity of the sample, R_t (in Kelvin per watt) must be known. This thermal resistance is the resistance of the sample. The output from the DAQ box must then be analyzed. It is known that a temperature change across a material is proportional to both the absolute thermal resistance and the heat flow through the sample,

$$\Delta T_{total} = P_{heat} \cdot R_{total} \quad (13)$$

where, ΔT_{total} is the absolute temperature difference (in Kelvin), P is the heating power through the material (in watts), and R_{total} is the total thermal resistance of the sample (in Kelvin per watt). To determine the temperature difference, the difference in temperature between the hot and cold temperatures is calculated by

$$\Delta T_{Total} = T_H - T_C \quad (14)$$

The average of these five hundred points is then taken, and the standard deviation, for reliability purposes, is taken. The heat flow through the material is the result of the heat generated by the heater attached to the bottom of the copper plate. Because the voltage and current are both displayed on the controller, the total power to the heater may be calculated with the formula

$$P_0 = V \cdot I \quad (15)$$

where, P_0 is the heating power (in watts), V is the voltage to the heater (in volts), and I is the current through the heater (in amperes). However, there are various heat losses through the wires and apparatus, and from the contact between the sample and the copper plates. Thus a correction factor must be applied to the power in equation 14. In considering this correction factor, the loss from the wiring and apparatus, given no modifications to the setup, is assumed to be proportional to the total power applied. Thus

$$P_{heat} = cP_0 \quad (16)$$

where P_{heat} is the power going through the sample (in watts), and c is a dimensionless proportionality constant. Furthermore, in considering correction factors, the offset of the thermocouples prior to measurements must be considered. With zero volts, no power is being

applied to the heater. Thus the original temperature difference for this voltage will be the offset of the two thermocouples, notes as

$$\Delta T_0 = T_H - T_C \quad (17)$$

where, ΔT_0 is the offset of the hot and cold thermocouples when $V=0$ volts (in Kelvin). Applying these offsets, the relationship between the temperature and the thermal resistance becomes

$$\Delta T_{total} - \Delta T_0 = (cP_0) \cdot R_{total} \quad (18)$$

At this point, there remain two unknowns, the proportionality constant c and the total resistance. However, the total resistance itself is a linear combination (series thermal circuit) of the resistance of the apparatus contacts and the loaded sample, or

$$R_{total} = R_C + R_S \quad (19)$$

where R_C is the apparatus thermal resistance (in Kelvin per watt), and R_S is the sample thermal resistance (in Kelvin per watt). This adds an additional unknown to equation (18), becoming

$$\Delta T_{total} - \Delta T_0 = (cP_0) \cdot (R_C + R_S) \quad (20)$$

To solve for the apparatus resistance, the resistance of the apparatus with no loaded sample, that is only the two copper plates, is tested. Since there is no sample being tested, the only resistance is the apparatus. The result is

$$\Delta T_{total} - \Delta T_0 = cP_0 \cdot R_C \quad (21)$$

where, c is the thermal conversion factor (dimensionless). Continuing on, a pure aluminum sample was measured at the various voltages (0, 2, 4, 6 and 8 volts). Because it is a pure material, the thermal conductivity is well known and established. Thus, the resistance, R_S , may be calculated from equation 22. Knowing this resistance and the various heater powers, a system of equations may be developed to solve for the two unknowns, the constant, c , and the apparatus thermal resistance R_C , as follows

$$\Delta T_{total-s} - \Delta T_{0-s} = cP_0 \cdot (R_C + R_S) \quad (22)$$

$$\Delta T_{total-c} - \Delta T_{0-c} = cP_0 \cdot R_C \quad (23)$$

Knowing the values of c and R_C , the thermal resistance for any sample may be readily calculated using the equations summarized in Table 7. This thermal resistance then allows the thermal conductivity at each voltage to be calculated. However, there is a certain level of deviation between voltage readings, thus the average of thermal conductivities for each power setting is averaged and recorded.

Table 7. Summary of fundamental equations for thermal conductivity calculations

Fundamental equations	Critical parameters and units
$R_t = \frac{L}{kA}$ $\Delta T - \Delta T^o = (R_S + R_C)(P_o - P_l)$ <p>where</p> $\Delta T = T_H - T_C$ $\Delta T^o = T_H - T_C \text{ (when } P_o = 0)$ $P_o = I \cdot V$	$k = \text{thermal conductivity} \left[\frac{\text{W}}{\text{m} \cdot \text{K}} \right]$ $L = \text{Length [m]}$ $A = \text{Cross sectional area [m}^2]$ $T_H = \text{Temp. of the hot side [K]}$ $T_C = \text{Temp. of the cold side [K]}$ $R_S = \text{Sample restistance [K/W]}$ $R_C = \text{Contact restistance [K/W]}$ $P_o = \text{Applied heating power [W]}$ $P_l = \text{Heating power leak [W]}$ $I = \text{Currrent [A]}$ $V = \text{Voltage [V]}$

3.1.2 Electrical Conductivity Equations

Electrical measurements were calculated directly from the measured resistance values from the digital multimeter. The output of this device is a resistance for the wires and sample combined. However, by connecting the alligator clips, the resistance of the wiring itself may be noted. This then acted as an offset for the measured electrical resistance values,

$$R_{\text{total}} = R_W + R_e \quad (24)$$

where, R_{total} is the measured electrical resistance (in ohms), R_{w} is the wiring electrical resistance (in ohms), and R_e is the sample's electrical resistance (in ohms). With R_{total} and R_{w} being measured directly, the sample's electrical resistance (R_e) may be determined.

The electrical resistance of a material is defined as

$$R_e = \frac{\rho L}{A} \quad (25)$$

where, ρ is the electrical resistivity of the material (in ohm-meters). Thus, knowing the length and area (see prior section), the resistivity may be solved for. The conductivity of a material is equivalent to the reciprocal of the resistivity. Thus

$$\sigma = \frac{1}{\rho} \quad (26)$$

where σ is the electrical conductivity of the material (measured in inverse ohm-meters). Thus, using the measured resistances from the four wire method, the conductivity of the material may be calculated, as summarized in Table 8. As this was performed for the thermal conductivity measurements, the average of the conductivity values for a given sample were taken and this average was the value produced for discussion.

Table 8. Fundamental equation for electrical conductivity calculations

Fundamental equation	Critical parameters and units
$R_e = \frac{\rho L}{A}$	$\rho = \text{resistivity } [\Omega \cdot \text{m}]$ $\rho^{-1} = \text{electrical conductivity } [\Omega^{-1} \cdot \text{m}^{-1}]$ $L = \text{Length } [\text{m}]$ $A = \text{Cross sectional area } [\text{m}^2]$ $R_e = \text{Sample resistance } [\Omega]$

3.2 Thermal Conductivity Measurements

The following sections describe the procedures used to conduct the thermal measurements for the different alloys including any prior preparation to the different samples. It also includes any changes or improvements made to the procedure throughout the course of the project and the justification for any of these. There are three main methods used for the thermal measurements since the beginning of the projects, they are presented in chronological order and display detailed information about how the data was taken.

3.2.1 Original Testing Procedure

Sample preparation was done using a series of sanding and polishing is performed to both faces of the sample, in progression from 200 to 400 to 600 to 1200. After polishing, a thin layer of thermal grease is applied to the two faces of the sample. The layer should have no visible residue, as it is only meant to fill the micro-cracks of the samples and copper plates.

Measurements were done using the following procedure. Each sample was placed in between the copper plates and then inserted into the smaller can as shown in Figure 24. The temperature controller was set at 31C for every trial. Measurements were taken for 0, 2, 4 and 6 volts. Originally the group believed that the sample needed 1.5 hours to reach equilibrium per every voltage setting to get the desired measurement information. For this testing procedure a copper/brass sample was used for as the calibration sample.

3.2.2 Modified Testing Procedure

After analysis was done on the data collected using the procedure outlined in the previous section, a new testing procedure was developed. Observing the behavior of the thermocouple we recognized that the difference in temperature was the same approximately 100 seconds after than it was 1.5 hours after the sample had been set up. This observation allowed us to reduce the interval of time in recording measurements.

The group was able to confirm this observation by selecting a one of our samples and recording data for five minutes, starting from zero seconds. Five minutes after the recording of data, 2 volts were applied to the sample and the spike was observed in the LabVIEW program. After this data was collected we then took measurements every 10 minutes. The data for this trial revealed that the sample reached equilibrium much faster that we had anticipated.

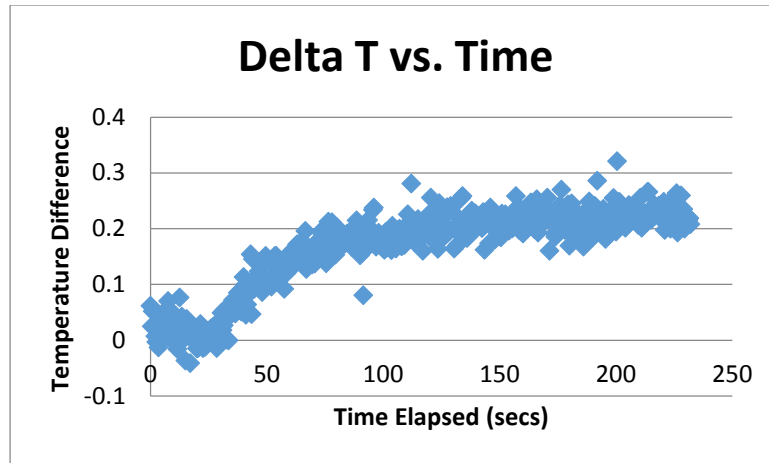


Figure 26. Plot of an Al 319 sample, showing the change in temperature with elapsing time before testing (while waiting for steady-state).

A third measurement procedure was developed to ensure better contact between the copper plates and the sample. The copper plates and wiring were kept the same way. This time a clamp was used to keep the copper plated on top of the samples being measured and the whole set up was placed inside a Styrofoam box to isolate the sample from other room conditions. This last procedure was used to collect the data used for the final analysis. Thermal measurements were conducted using the apparatus discussed earlier.

In loading the sample, the sample is placed in the center of the lower copper plate. The top plate is then placed in the middle of the sample. This setup is then placed in a Styrofoam container for insulation purposes. A rod is then placed through a metal clamp to apply pressure to the top of the plate to prevent any shifting of the sample and to ensure a high level of contact between the sample and the plates.

Once loaded, any extra lengths of thermocouples are secured underneath a block of lead to lower the variation in temperature throughout the wire length. This setup is then covered with a layer of foam, and finally a plastic sheet to block any currents which may be in the room. The physical sample is henceforth setup.

Using the computer program, a visual inspection should be made to determine when all three thermocouples have reached ambient temperature. They should be roughly within 0.1 Kelvin of each other and the temperature should be at a steady state. Data is then recorded for a 250 second period, saved to a file, and appropriately labeled. The voltage must then be increased

from 0V to 2V for the heater. A time interval must then be waited for the two sides of the plate to begin heating. Once the slopes of the hot and cold thermocouple are equal (after roughly five or ten minutes), the next 250 second measurement may be taken. Again this result is saved and then next reading, may begin. The same procedure is followed for the next reading, going from 2V to 4V, then 4V to 6V, and finally 6V to 8V. At this point the sample has been fully measured and may be unloaded. Note the power controller must be set to 0V for the loading of the next sample.

3.3 Electrical Conductivity Measurements

Electrical measurements on the samples were conducted using a digital multimeter with a 4-wire measurement technique. A 4-wire measurement involves using separate pairs of current and voltage carrying electrodes. The 4-wire measurement minimizes the contact and wire resistance measured by the multimeter and ensures that the resistance measured is the actually the electrical resistance of the sample. In order to ensure a good contact between the sample and the leads, the sample was clamped to the leads. Rubber pads were placed between the ends of the clamp and the leads in order to isolate the leads from the clamps electrically.



Figure 27. Four wire electrical measurement setup.

3.4 Data Collection and Analysis

After data was taken for the samples anomalous thermal resistance readings were noted. There were three sources of anomalous thermal resistance measurements. The first was that the data for the individual sample run exhibited an exponential increase in the difference in temperature between the top and bottom plates. The samples selected were checked for surface flatness, reproducibility and consistent testing conditions. The results shown were obtained by averaging the values of the reliable runs for samples of the same category.

Chapter 4: Results and Discussion

4.1 Effects of Aging Time on Thermal and Electrical Conductivities

Using the fundamental equations outlined in Section 3.1.1. The team was able to calculate thermal conductivities for the all samples tested. Data analysis revealed a specific trend relating thermal conductivity and aging time. It was found that as aging time in 6061 samples increased, thermal conductivity increased as well. The 6061 sample in the T4 condition with 0 hours of aging time showed the lowest value of thermal conductivity at 141 W/(m*K). The highest value was for the T6 16 hour sample with a thermal conductivity of 191 W/(m*K). As Figure 28 shows, an upward trend is observed as aging time increases.

The increased thermal conductivity observed in the 6061 samples is a result of the precipitates that have formed over time. The precipitates at the T6 condition are fully blown and have clustered in specific locations, which make the α -Al matrix leaner. This allows for the signal going through the 6061 sample to start flowing faster, and ultimately results in higher thermal conductivity. As aging time increases the precipitates grow bigger, leaving open channels in the matrix for the signal to travel through.

The results also showed that 6061 and A356 had higher thermal conductivities than 319. This is due to the presence of copper in the α -Al matrix, due to the chemical composition of 319. This addition makes it more difficult for the signal to travel through the sample when compared to 6061 and A356. The presence of copper changes the strengthening precipitate system by the presence of Al-Cu and Al-Cu-Mg-Si precipitates. These additional precipitates disrupt the transfer of the thermal signal through the α -Al matrix and reduce thermal conductivity.

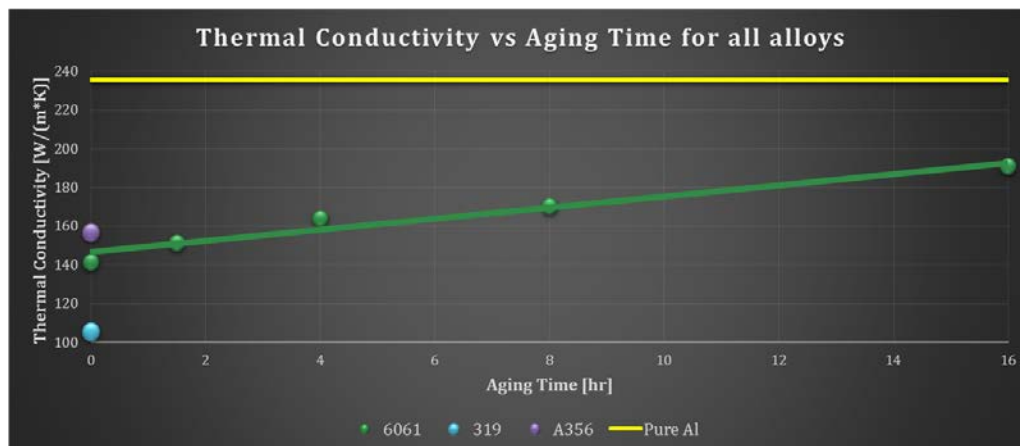


Figure 28. Relationship between thermal conductivity and aging time in all alloys.

Like the thermal conductivity, the electrical conductivity of 6061 increases with aging time, Figure 29. The mechanism for the increase in electrical conductivity is the same as the one for increase in thermal conductivity. That is aging causes the Si precipitates in the alloy to cluster tightly together leaving the α -Al matrix leaner and allowing an electrical signal to more easily propagate through it.

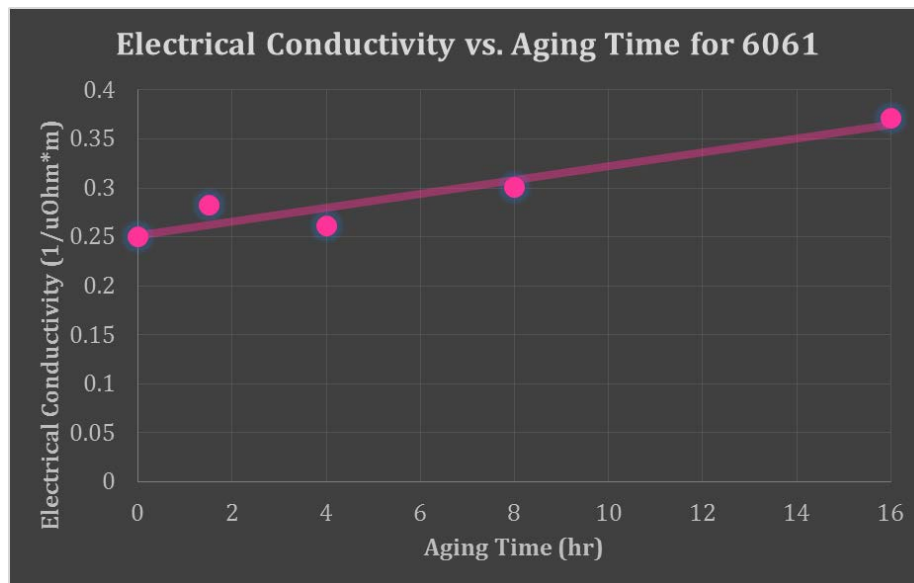


Figure 29. Relationship between electrical conductivity and aging time in 6061.

4.2 Effects of SDAS on Thermal Conductivity

From the results of the conductivity measurements, it was determined that as secondary dendrite arm spacing increases, the conductivity of the material also increases. For the A356 data set it was experimentally found that increasing SDAS from 60 μm to 100 μm produces an increase from 160 $\text{W}/(\text{m}\cdot\text{K})$ to 180 $\text{W}/(\text{m}\cdot\text{K})$ (see Figure 30.). This is because, as can be seen from the two micrographs, as the spacing increases, the size of the α -aluminum regions increases. By having larger pure aluminum regions, electrons, the particles which carry thermal energy, have more continuous movement paths, having less silicon dendrite obstructions.

As dendrite arm spacing increases (solidification time is longer and dendrites have a longer time to grow), higher thermal conductivity is observed, given that larger SDAS are associated with larger α -Al regions and coarser spacing of the Si particles in the eutectic areas, as seen in Figure 30. Given that α -Al matrix is the dominant transport pathway in the material, the electrical conductivity is expected to follow a similar trend.

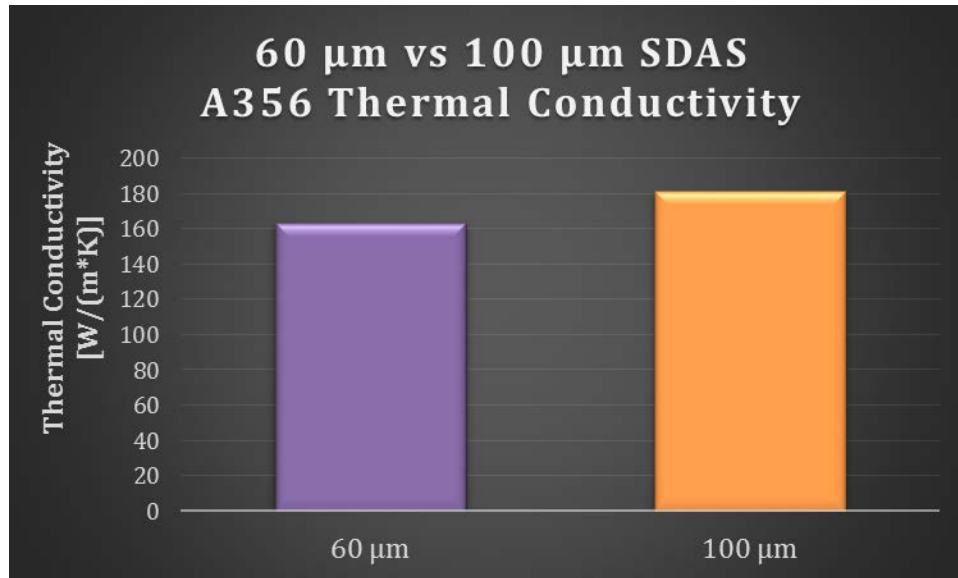


Figure 30. Relationship between thermal conductivity and SDAS in A356.

4.3 Effects of Eutectic Si Modification on Thermal Conductivity

From the results shown in Figure 31 and Figure 32, both 319 and A356 Sr modified alloys exhibit a lower thermal conductivity than the unmodified alloys. The decrease in the thermal conductivity in the alloys is a result of the finer and closer-spaced distribution of Si particles that exist in the eutectic regions of the materials.

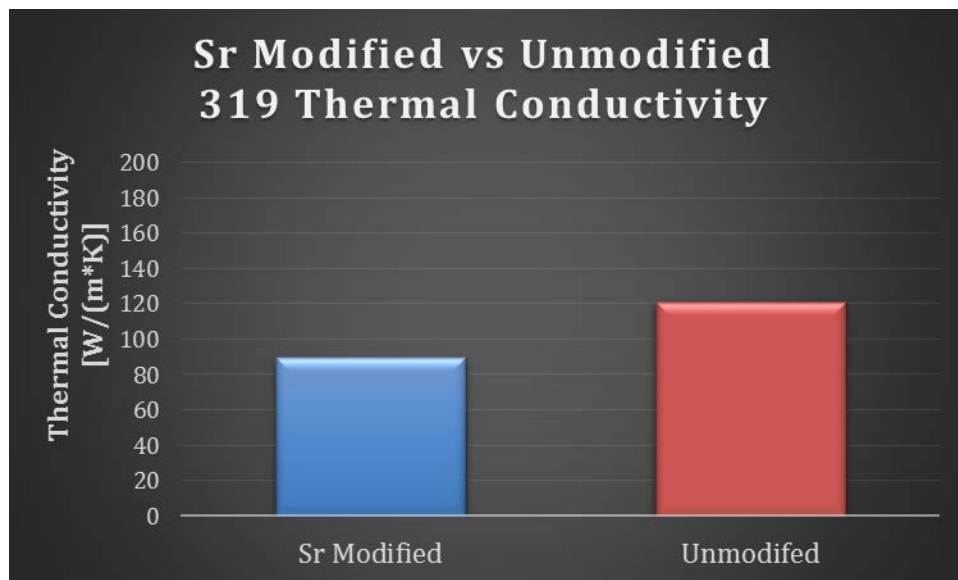


Figure 31. Relationship between thermal conductivity and Sr modification in A319.

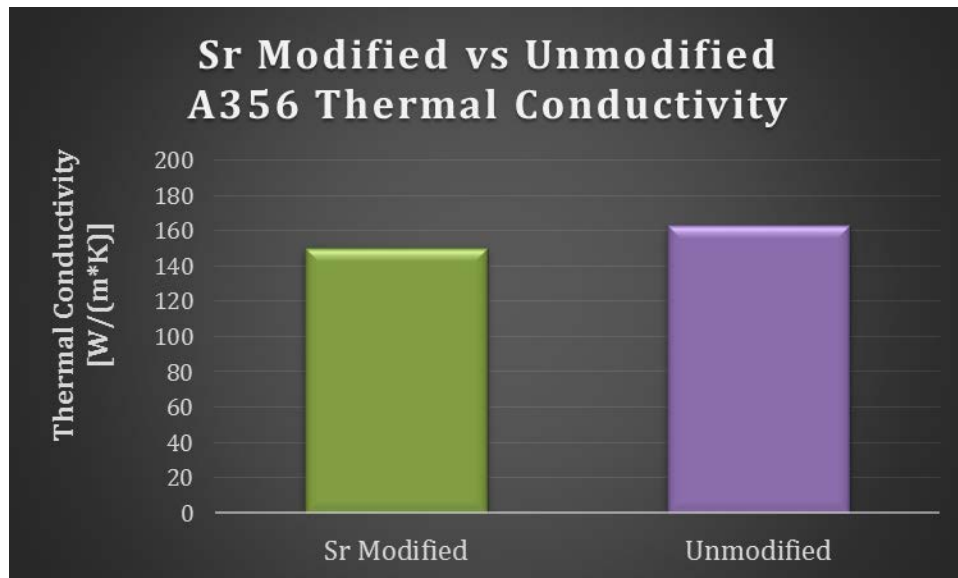


Figure 32. Relationship between thermal conductivity and Sr modification in A356.

4.4 Correlation between Thermal Conductivity and Microhardness

Vickers microhardness tests were conducted, and the results were correlated with thermal conductivity. As microhardness increases thermal conductivity also increases. This is due to the mechanisms behind the increase in microhardness of 6061. The growth in precipitates in 6061 causes dislocations to require increasing amounts of energy to propagate through the material, increasing the strength of the alloy. This same growth in the precipitates also causes the α -Al matrix to become “leaner” in alloying elements, which allows for easier passage of the thermal signal through it.

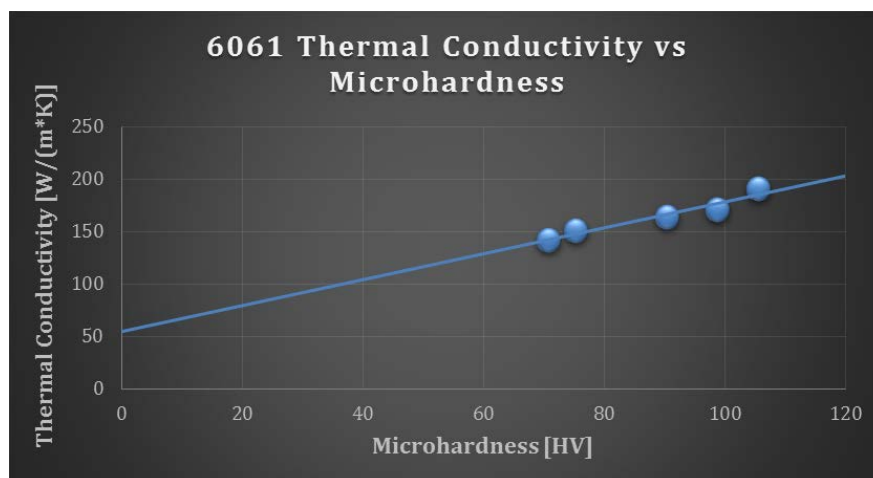


Figure 33. Relationship between thermal conductivity and microhardness in 6061.

For this relation the Vickers test was used as a method to find the matrix microhardness of the samples. The test consists of a very small diamond indenter, shaped as a pyramid with a square base and an angle of 136° . This diamond is forced into the surface of a material sample. The load for this particular test usually range between 1 and 1000g and applies for a time period ranging from 10-15 seconds. Actual measurements were conducted with a 100g load for 10 seconds. After the load is applied to the sample, the indentation is measured and analyzed with a microscope. After this measurement is obtained as a ratio, it is then converted into a hardness number. For this test the Law of proportional resistances is applicable, where the force and surface indentation are proportional. In order to calculate a hardness value (HV), you need to know the load being applied P , and the average distance of the diagonals. In this case P is usually in kg and d is in mm. This can be seen in Figure 34 which shows the geometry of the indenter and the diagonals that are mentioned above (Callister, 2000).



Figure 34. Shape of indentation side view and top view in a typical Vickers microhardness test (Callister, 2000).

The formula to calculate the hardness number is outlined below:

$$HV = \frac{P}{A} = \frac{1.854 \times P}{d_1^2}. \quad (27)$$

4.5 Eutectic Particle Size and Shape Factor Relationships to Thermal Conductivity

Table 9 shows measurements of the equivalent particle diameter and the shape factor of the eutectic silicon particles. Sr modification in 319 and A356 produces a smaller particle size and increased shape factor. A finer and more uniform distribution of Si particles within the eutectic regions was also observed in the Sr modified samples versus the unmodified samples.

Table 9. Particle size and shape factor of 319 and A356 alloys

Eutectic Si particle		319 Unmodified (60 μm SDAS)	319 Sr Modified (60 μm SDAS)	A356 Unmodified (60 μm SDAS)	A356 Unmodified (100 μm SDAS)	A356 Sr Modified (60 μm SDAS)
Diameter [μm]		3.17	2.38	4.46	5.61	1.32
Shape Factor		0.504	0.795	0.495	0.468	0.876

Figure 35 and Figure 36 show the relationship between thermal conductivity and Si particle size and shape factor. In general within the same alloy, an increase in thermal conductivity is associated with increased eutectic Si particle size. Conversely, increases in thermal conductivity are associated with decreases in shape factor. Sr modification produces smaller Si particles with a higher shape factor, and also produces a finer and more uniform distribution within the eutectic regions themselves.

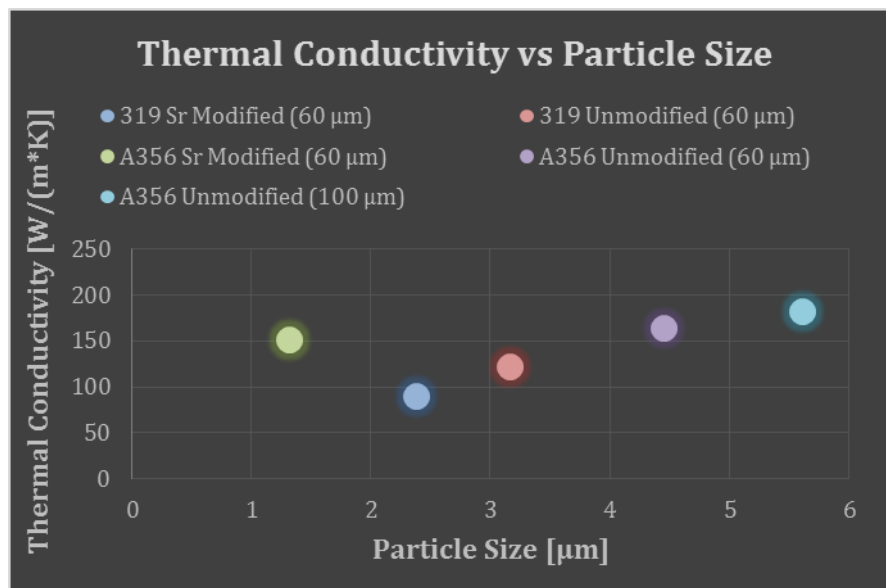


Figure 35. Relationship between thermal conductivity and eutectic Si particle size for 319 and A356 cast alloys.

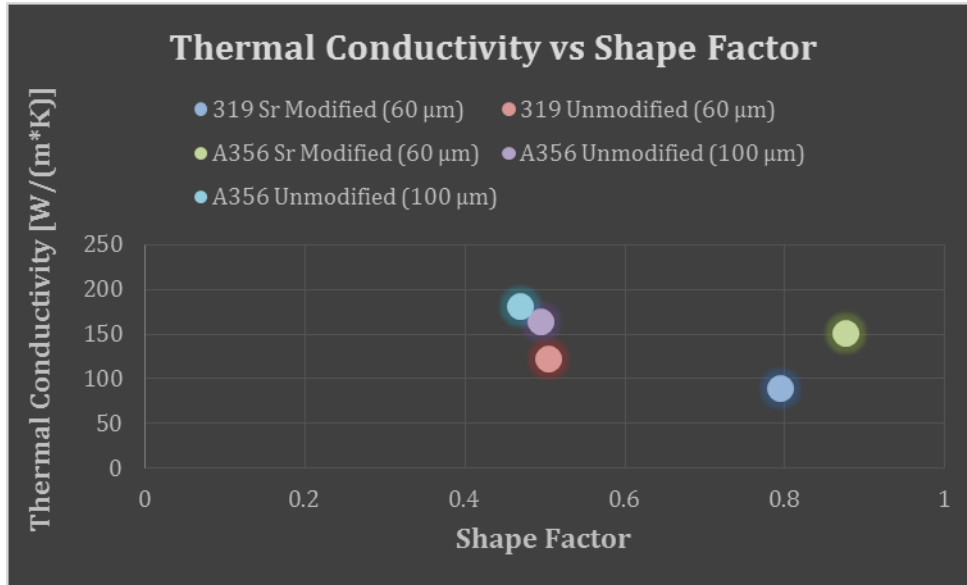


Figure 36. Relationship between thermal conductivity and eutectic Si shape factor for 319 and A356 cast alloys.

Chapter 5: Conclusions, Recommendations and Future Work

5.1 Conclusions

Based on the experimental results, it has been shown that there is a relationship between the aging time of 6061, A356, and 319 alloys and their thermal and electrical conductivities. In conclusion, it has been proven that as aging time increases from 0 hours in the T4 condition to 16 hours in the T6 condition, the thermal conductivity of 6061 increases. This is caused by the formation of the precipitates in the alloys as aging time increases. Electrical conductivity also shows an upward trend when compared with aging time. In the initial stages of aging, there is an increase in thermal conductivity for a brief amount of time, followed by a decrease with increasing aging time. The formation of precipitates causes the α -Al matrix to be leaner in alloying elements such as Mg and Cu. In comparison to the 6061 and A356 alloys, the 319 alloys have a lower thermal conductivity. This is a result of the number of Cu particles in the 319 alloys. 319 alloys have a larger amount of Cu particles in the α -Al matrix.

In terms of eutectic Si modification in these alloys and their respective secondary dendrite arm spacing, these characteristics affect their thermal conductivities. It can be concluded that A356 and 319 alloys with strontium additions have a lower thermal conductivity than those that are unmodified due to their silicon distribution in the eutectic regions. It can also be concluded that alloys with larger secondary dendrite arm spacing have a higher thermal conductivity due to their large α -Al regions.

5.2 Recommendations and Future Work

Based on experiment, a number of recommendations have been made to improve the experimental procedure for future work. To gain a better understanding of transport phenomena in materials, the existing methodology could be applied to other aluminum alloys as well as other metal alloys. A wider range of heat treatments could be explored as well. To improve thermal measurements, the uniformity of the contact between the samples and the copper plates could be improved to ensure that methods remain consistent throughout numerous trials. An improved system of thermal insulation could be applied to the apparatus as well. A wider range of temperatures could be explored by making a comparison between measurements conducted at room temperature to those conducted at extremely high temperatures. To explore different

methods of aging and make more correlations to the thermal and electrical conductivity of the samples, they could be aged in-situ inside of the test apparatus.

References

- Akhil, K., Arul, S., & Sellamuthu, R. (2015). The Effect of Heat Treatment and Aging Process on Microstructure and Mechanical Properties of A356 Aluminum Alloy Sections in Casting. *Procedia Engineering*, 97, 1678-1682.
- ASM International. (1991). Properties of Wrought Aluminum and Aluminum Alloys. In *ASM Handbook* (pp. 62-122). Russell Township: ASM International.
- Bakhtiyarov, S. I., Overfelt, R. A., & Teodorescu, S. G. (2001). Electrical and thermal conductivity of A319 and A356 aluminum alloys. *Journal of Materials Science*, 36, 4643-4648.
- Bogdanoff, T., & Dahlstrom, J. (2009). The influence of copper on an Al-Si-Mg alloy (A356) - Microstructure and mechanical properties. *Jonkoping University School of Engineering*.
- Boudenne, A., Ibos, L., Fois, M., Majesté, J., & Géhin, E. (2005). *Electrical and thermal behavior of polypropylene filled with copper particles*.
- Cahill, D. G. (n.d.). *Measurement of thermal conductivity*. Retrieved from Department of Materials Science University of Illinois at Urbana-Champaign: http://users.mrl.illinois.edu/cahill/thermal_school09.pdf
- Cerri, E., Evangelista, E., Sprigarelli, S., Cavaliere, P., & DeRiccardis, F. (2000). Effects of thermal treatments on microstructure and mechanical properties in thixocast 319 aluminum alloy. *Materials Science and Engineering: A*, 284(1), 50-62.
- Collaboration for Nondestructive Testing Education. (2012). *Solidification*. Retrieved from NDT Resource Center: <https://www.nde-ed.org/EducationResources/CommunityCollege/Materials/Structure/solidification.htm>
- Davidson, M. (1997). *Searle's bar method for a good heat conductor*. Retrieved from media.paisley.ac.uk/~davison/labpage/searle/searle.html
- Davis, J. R. (Ed.). (1993). *Aluminum and Aluminum Alloys*. ASM International.
- Ernst, F. (2004). *Precipitation Hardening of Al-Si-Mg Alloys*. Cleveland: Case Western Reserve University.
- Essers, E. (2003). *United States of America Patent No. 6,590,210*.
- Gibbs-Thomson equation*. (2004, October 30). Retrieved from Wikipedia: http://en.wikipedia.org/wiki/Gibbs%E2%80%93Thomson_equation

- Gladman, T. (1999). Precipitation hardening in metals. *Materials Science and Technology*, 15(1), 30-36.
- Gopikrishna, S., & Yeldose, B. (2013). Study on effects of T6 heat treatment on grain refined A319 alloy with Magnesium and Strontium addition. *International Journal on Theoretical and Applied Research in Mechanical Engineering*, 2(3), 59-62.
- Grandfield, J., & Eskin, D. G. (2013). *Essential Readings in Light Metals, Cast Shop for Aluminum Production*. Hoboken, New Jersey: John Wiley & Sons, Inc.
- Grieve, D. (2003, January 23). *Aluminum Castings*. Retrieved from <http://www.tech.plym.ac.uk/sme/mech330/alcast1.htm>
- Grigoriev, S., Tarasova, T., Gvozdeva, G., & Nowotny, S. (2013). Structure formation of hypoeutectic Al-Si-alloys produced by laser surface treatment. *Strojniški Vestnik – Journal of Mechanical Engineering*, 389-394.
- Havill, J., & Thuo, S. (2014). *Thermal and Electrical Transport*. Worcester.
- Hernandez-Paz, J. F. (2003). Heat Treatment and Precipitation in A356 Aluminum Alloy. McGill University.
- Kaufman, J. G., & Rooy, E. L. (2004). *Aluminum Alloy Castings: Properties, Processes, and Applications*. ASM International.
- Key to Metals AG. (2010, January). *Precipitation Hardening of Aluminum Alloys :: Total Matera Article*. (Key to Metals AG) Retrieved October 19, 2014, from <http://www.keytometals.com/page.aspx?ID=CheckArticle&site=ktn&NM=235>
- Lombardi, A., Elia, F. D., Ravindran, C., Murty, B. S., & MacKay, R. (2011). Analysis of the secondary phases in the microstructure of 319 type Al alloy engine blocks using electron microscopy and nanoindentation. *The Indian Institute of Metals*, 7-11.
- Malekan, M., & Shabestari, S. G. (2009). Effect of Grain Refinement on the Dendrite Coherency Point during Solidification of the A319 Aluminum Alloy. *Metallurgical and Materials Transactions A*, 40(13), 3196-3203.
- Manzano-Ramirez, A., Nava-Vazquez, E., & Gonzalez-Hernandez, J. (1993). Electrical-conductivity and microstructure of aluminum alloys. *Metallurgical Transactions - A Physical Metallurgy and Materials Science*, 24(10), 2355-2358.

- Merlin, M., & Garagnani, G. L. (n.d.). Mechanical and microstructural characterisation of A356 castings realised with full and empty cores. *University of Ferrara Department of Engineering*.
- Mukhopadhyay, S. M. (2003). *Sample Preparation for Microscopic and Spectroscopic Characterization of Solid Surfaces and Films*. Retrieved from Sample Preparation Technique in Analytical Chemistry:
http://www.spectroscopynow.com/userfiles/sepspec/file/specNOW/Tutorials/sample_prep_mitra_377-412.pdf
- Murugan, N., Christy, T., & Kumar, S. (2010). A Comparative Study on the Microstructures and Mechanical Properties of Al 6061 Alloy and the MMC Al 6061/TiB₂/12P. *Journal of Minerals and Materials Characterization and Engineering*, 57-65.
- Nave, C. R. (1998). *Resistance and Resistivity*.
- Nave, C. R. (2000). *Thermal Conductivity and the Wiedemann-Franz Law*. Retrieved April 15, 2015, from <http://hyperphysics.phy-astr.gsu.edu/hbase/thermo/thercond.html>
- Pace Technologies. (2014). *Introduction to Metallography*. Retrieved from Pace Technologies:
<http://www.metallographic.com/Technical/Metallography-Intro.html>
- Rao, D. H., Tagore, G. R., & Janardhana, G. R. (2010). Evolution of Artificial Neural Network (ANN) model for predicting secondary dendrite arm spacing in aluminum alloy casting. (A. E. Diniz, Ed.) *Journal of the Brazilian Society of Mechanical Sciences and Engineering*, 32(3).
- Shabani, M., Mazahery, A., Bahmani, A., Davami, P., & Varahram, N. (2010). Solidification of A356 Al alloy: Experimental study and modeling. *Metallic Materials*, 253-258.
- Smith, C. (1935). *The Relation Between the Thermal and Electrical Conductivities of Copper Alloys*. Physical Review.
- TA Instruments. (2012). *Principal Methods of Thermal Conductivity Measurement*.
- Tham, Y., Fu, M., Hng, H., Pei, Q., & Lim, K. (2007). Microstructure and Properties of Al-6061 Alloy by Equal Channel Angular Extrusion for 16 Passes. *Materials and Manufacturing Processes*, 819-824.
- Vazquez-Lopez, C. (1999). Influence of dendrite arm spacing on the thermal conductivity of an aluminum-silicon casting alloy. *Journal of Materials Research*.

- Venkanna, B. K. (2010). *Fundamentals of Heat and Mass Transfer*. New Delhi: PHI Learning Private Limited.
- Wang, H., & Lo, S. (1996). Effects of aging on the thermal conductivity of silicon carbide particulate reinforced 6061 aluminum composite. *Journal of Materials Science*, 15, 369-371.
- Wang, H., Liu, J., Zhang, X., & Takahashi, K. (2013). Breakdown of Wiedemann-Franz law in individual suspended polycrystalline gold nanofilms down to 3 K. *International Journal of Heat and Mass Transfer*, 66, 585-591.
- Wikimedia Foundation. (2014, October 29). *Thermal Conductivity Measurement*. Retrieved from Wikipedia: http://en.wikipedia.org/wiki/Thermal_conductivity_measurement
- Woodcraft, A. L. (2005). Predicting the thermal conductivities of aluminum alloys in the cryogenic to room temperature range. *Cryogenics*, 45(6), 421-431.